CZECH TECHNICAL UNIVERSITY IN PRAGUE
Faculty of Nuclear Sciences and Physical Engineering

Diploma thesis

Aspects of energy calibration of cosmic ray showers detected by surface detector at the Pierre Auger Observatory

Jakub Vícha

Prague, 2010

Prohlášení

Prohlašuji, že jsem svou diplomovou práci vypracoval samostatně a použil jsem pouze podklady (literaturu, projekty, SW atd.) uvedené v přiloženém seznamu.

Nemám závažný důvod proti užití tohoto školního díla ve smyslu § 60 Zákona č.121/2000 Sb., o právu autorském, o právech souvisejících s právem autorským a o změně některých zákonů (autorský zákon).

V Praze dne ________________

____
podpis

PIERRE
AUGER
OBSERVATORY

Acknowledgements

I am very grateful to RNDr. Petr Trávníček, PhD. for conscientious corrections in this thesis and also for discussions about studied problematic. Further, I thank Ing. Michal Nyklíček for technical supports. I am also very grateful for support of my family and my girlfriend during study.

Aspects of energy calibration of cosmic ray showers detected by surface detector at the Pierre Auger Observatory

Author: Jakub Vícha

Field of study: Nuclear engineering

Specialization: Experimental nuclear physics

Type of work: Diploma thesis

Supervisor: RNDr. Petr Trávníček, PhD., Institute of Physics AS CR

Consultant: Ing. Michal Nyklíček, Institute of Physics AS CR

Abstract

The project Pierre Auger Observatory researches cosmic rays of ultra-high energies via measurement of produced extended showers in atmosphere. The Observatory utilizes events detected simultaneously by two independent detection techniques to calibrate signals obtained from surface detector (SD) field to precise energy measurement given by fluorescence detector (FD). This process proceeds in two steps involving drawing of two curves. The first one, the attenuation curve, is a outcome of Constant Intensity Cut method and the second one is a resulting calibration curve of SD signal in relation to the FD energy. Various aspects including dependencies of these curves on chosen selection cuts, seasonal atmospheric effects and position of shower maximum were studied. Stability of these curves was confirmed and quantified. Existence of mixed chemical composition of primary cosmic rays above 3 EeV helps to explain behaviour of calibration curve for showers with small and large depths of shower maxima.

Keywords: Cosmic ray showers, energy calibration, surface detector, X_{max}, chemical composition.

Aspekty kalibrace energie spršek kosmického záření při detekci povrchovým detektorem na Observatoři Pierra Augera

Autor: Jakub Vícha

Obor zaměření: Jaderné inženýrství

Specializace: Experimentální jaderná fyzika

Typ práce: Diplomová práce

Školitel: RNDr. Petr Trávníček, PhD., Fyzikální ústav AV ČR

Konzultant: Ing. Michal Nyklíček, Fyzikální ústav AV ČR

Abstrakt

Projekt Observatoř Pierra Augera se zabývá studiem kosmického záření o ultra vysokých energiích pomocí spršek sekundárních částic produkovaných v atmosféře. Observatoř využívá událostí detekovaných nezávisle dvěmi detekčními technikami ke kalibraci signálu z pole povrchových detektorů (SD) pomocí přesně změřené energie fluorescenčním detektorem (FD). Tento proces probíhá ve dvou fázích, při kterých se získávají dvě křivky. První z nich, útlumová křivka signálu povrchového detektoru, je výsledkem použité Metody toku konstantní intenzity a druhá již popisuje závislost signálu z SD na energii měřené v FD. V práci byly zkoumány různé aspekty kalibračního procesu zahrnující závislosti těchto křivek na výběrových podmínkách při jejich tvoření, sezónních vlivech atmosféry a na pozici maxima spršky. Stabilita těchto křivek byla potvrzena a kvantifikována. Projev závislosti kalibrační křivky na pozici maxima spršky může být vysvětlen za předpokladu smíšeného složení kosmického záření o energiích větších než 3 EeV.

Klíčová slova: Kosmické záření, energetická kalibrace, povrchový detektor, X_{max}, chemické složení.

Contents

Chapter 1

Introduction

Although human made accelerators like Large Hadron Collider (LHC) provide interesting knowledge about high energy particle physics, the "cosmic accelerators" are able to induce particles of energy 7 orders in magnitude larger than it is expected to be achieved at LHC (100 EeV vs. 7 TeV). This energy is related to the laboratory system (LS) but for particle interactions the energy of collision in the central mass system (CMS) has more relevant information. For comparison, the energy of 10^{20} eV cosmic proton collision with air molecule in CMS exceeds the mentioned LHC energy of proton-proton collision more than one order of magnitude. Thus to make some assumptions about interactions of ultra high energy cosmic rays (UHECR), which covers the region of energy $\gtrsim 10^{18}$ eV [1], it is necessary to use extrapolations from accelerator's data [2]. However, the mass-range of so far discovered hadrons extends about 4 orders of magnitude, which indicates that various interaction effects of so far unknown heavy particles may occure in the region of UHECR. Data from cosmic ray experiments indeed show discrepancies in confrontation with such extrapolations. A question arrises to which extend models of particle interaction and production can be constrained by cosmic ray experiments at energies far beyond accelerator capabilities.

Production of extremely high energy cosmic rays (EHECR) with energy above $5{\cdot}10^{19}$ eV remains mystery already for 40 years. Therefore there is strong particle physics motivation for studying cosmic rays although the biggest interest in particle physics rests mostly on accelerator's physics shoulders.

The flux of EHECR is so small that even detector of fully efficient surface of 1 km^2 placed in space vacuum would detect probably only one such particle during whole century of measurement. Thus it is necessary to detect UHECR indirectly through extended showers of secondary particles induced by primary cosmic rays in the Earth atmosphere. For these and further reasons the project of Pierre Auger Observatory (PAO) was built to reveal secrets which are surrounding the mystery of the most energetic cosmic rays.

[1] All following energies are related to the LS.

[2] Nowadays, data from Tevatron (1 TeV in CMS) are at disposal, which is below EHECR even more than 2 orders in magnitude.

This thesis describes PAO more concretely and especially it is devoted to the energy calibration of the surface detector field and various influencing aspects.

In the second chapter basic characteristics of UHECR and reasons for studying them are presented. The third chapter describes Pierre Auger Observatory more concretely and points out its most important scientific results. Further two chapters comprise author's original results: the fourth chapter deals with energy calibration of PAO and in the fifth chapter various influencing aspects of energy calibration of the surface detector are discussed. The last chapter summarises obtained results.

Chapter 2

Goals and Puzzles of Studying Cosmic Rays of Highest Energies

The main questions of cosmic ray physics are where are cosmic rays coming from, what is their composition, at which rate and how are they produced? For particles of energy up to UHECR energies these questions are somehow satisfactorily answered and generally accepted, but for origin of UHECR there are many ways of explanations. Some features of cosmic ray shower, which have to be taken under consideration to formulate answers to these questions, are pointed out in this chapter. The chapter concentrates also on selected aspects of cosmic ray particle acceleration and puzzles of the existence of UHECR and EHECR particles.

2.1 Shower Development

The idea of UHECR detection lies in the use of atmosphere as a huge calorimeter and measurement of the shower of secondary particles induced by the primary particle of cosmic rays as it reaches the atmosphere. The shower naturally undergoes certain development and in the first approximation it can be described as a disc with variable size moving in the atmosphere to the Earth. This size is proportional to the number of secondary particles. The normal direction of the disc represents the so called shower axis that is considered to be very similar to the original direction of the primary particle. The intersection of the shower axis with ground is known as the shower core.

The shower of secondary particles may be decomposed into three parts as it is depicted in Fig. 2.1. Heavier particles remain mainly near the shower axis and so this region is named hadronic core as it contains hadrons such as protons, neutrons, kaons, pions and nucleus fragments. This "near" collimation is caused by little deviated scattering due to large masses of hadrons. Another part of the shower is the electromagnetic component which contains photons and electrons with positrons. This huge and widely spread electromagnetic cascade is mainly feeded by photons emerging from decays of π^0. It consists of ionised electrons, produced electron-positron pairs and radiative photons. Due to wide angle scattering of light electrons this shower component is spread very widely. The last shower segment is called the hard component of shower. It contains muons that penetrate mostly up to the Earth surface and the most energetic ones even far below the surface. Into hard component also neutrinos belong. They naturally escape undetected.

Charged shower particles excite nitrogen molecules and the excited molecules emmit detectable fluorescence light. Moreover shower particles moving with velocities greater than the speed of light in air produce directed Cherenkov light that contamines detected fluorescence light. During deposition of the shower electromagnetic energy in the atmosphere radio- and micro-waves are produced, which may also be used as a basis of possible detection technique.

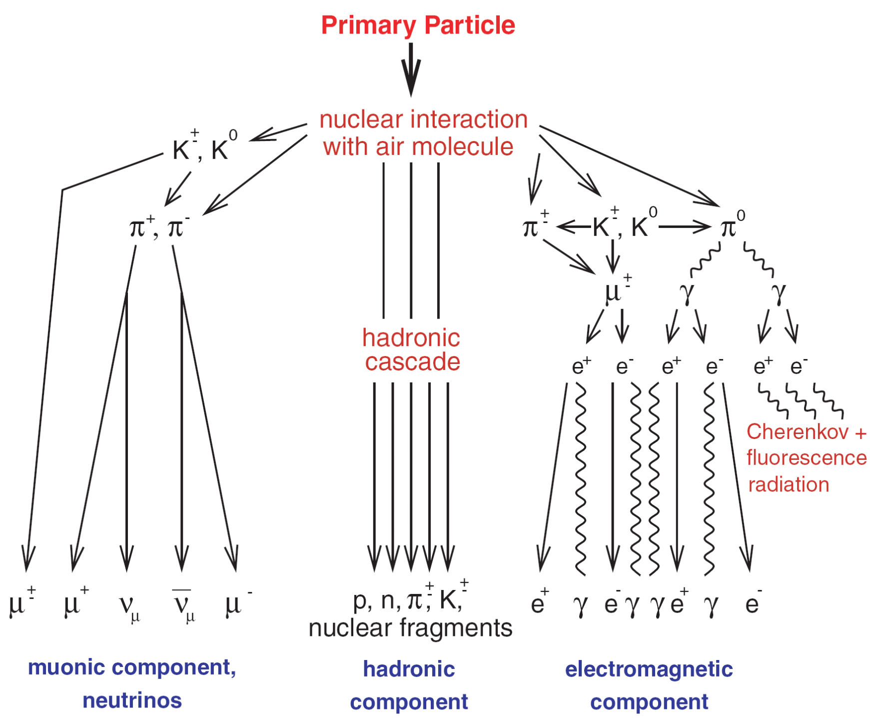

Figure 2.1: Composition of cosmic ray shower induced by primary particle. Picture is taken from [1].

The first interaction of UHECR primary particle, according to simulations, occurs between 30 and 40 km. Besides event-to-event fluctuations, the position of the first interaction depends on type of primary particle. By the assumption that UHECR are hadrons, especially stable nuclei of atoms from periodic table up to iron, the collision of cosmic nucleus with nucleus in the atmosphere can be considered as the interaction of indenpendent nucleons of primary cosmic particle. This is the so called eikonal approximation of Glauber model and more information may be found in [2]. In a simplyfied way, for heavier nucleus there is a greater probability of interaction than for lighter ones, since the heavier nuclei are composed of more nucleons which are all able to interact with the same probability. Therefore it is expected that lighter UHECR penetrate deeper in the atmosphere.

Secondary particles loose their energy during the shower development by elastic and inelastic collisions with air molecules, by their decays and by production of Cherenkov light or radiative photons.

The number of secondary particles naturally grows up after the first collision but there has to be some critical point of shower development after which the particles have not sufficient energy for production of new particles or they are stopped due to ionisation losses. After the critical point number of secondary particles decreases. The position of this critical point of shower development depends, neglecting stochastic fluctuations, on the energy of the primary particle and also on the position of its first interaction. The quantity describing this critical point, and depending on mass composition, is labeled as X_{max}. This quantity reflects the mass of the atmosphere through which the cosmic ray shower has to penetrate to reach the critical point of the shower development. This point of shower development (at altitude l_{max}) corresponds to the situation when the shower contains the largest number of secondary particles. X_{max} is defined as

$$X_{max} = \int_{l_{max}}^{\infty} \frac{\rho(l)}{cos(\Theta)}\, dl \tag{2.1}$$

where $\rho(l)$ describes the air density at the altitude l and Θ is the zenith angle of the shower axis. As unit for X_{max} mostly g·cm^{-2} is used. Measuring X_{max} and shower energy simultaneously the mass composition of cosmic rays can be studied.

2.2 Mass Composition

Generally, cosmic rays of energies above 10^8 eV [1] are formed primarily by protons (90 %) and helium nuclei (9 %). Only about one percent is assigned to heavier nuclei and the rest minuscule part represents photons, electrons and neutrinos. Due to indirect detection of UHECR via extended air showers it is very problematic to measure their mass composition. This is caused by lesser statistical data set in this energy region (especially for EHECR) and mainly due to the fact that results have to be compared with simulations which, as it was indicated earlier, are based on extrapolations of accelerators data to ultra-high energies.

Mostly charged nuclei are assumed as primary UHECR particles, since only accelerating mechanisms based on electromagnetic fields are considered. Theoretical physicists are still unable to satisfactorily explain accelerating processes producing particles of such high energies. Thus how EHECR origin is one of the uncovered physics mysteries waiting for reveal.

2.3 Origin and Propagation in Extragalactic Space

Together with mass composition also propagation of primary cosmic ray particles is connected to their origin. It is generally accepted that in our Galaxy only particles below UHECR energies are produced and UHECR originate outside our Galaxy. The main effect influencing direction of UHECR propagation is their bending in magnetic fields. The scattering angle δ of particle of charge $Z \cdot e$ with

[1] Cosmic ray particles originating outside our solar system with lower energies are blowed off the solar system by solar wind and thus they are not considered.

energy E traveling distance d in magnetic field of intensity B is proportional to $\sim d/r_L$ where the curvature r_L is the so called Larmor radius satisfying the equation

$$r_L[kpc] = \frac{E[EeV]}{ZeB[\mu G]} \,. \tag{2.2}$$

Considering proton of energy [2] 1 EeV moving in magnetic field of intensity 3 μG, Larmor radius equals to 300 pc, which is approximately the thickness of our Galaxy disc. Therefore only for particles of energy over $\sim 10^{19}$ eV it is appropriate to search for anisotropy of their arrival directions, and thus for possible sources. Extragalactic proton of smaller energy is too much bent in magnetic field of our Galaxy, that the information about the proton direction is lost.

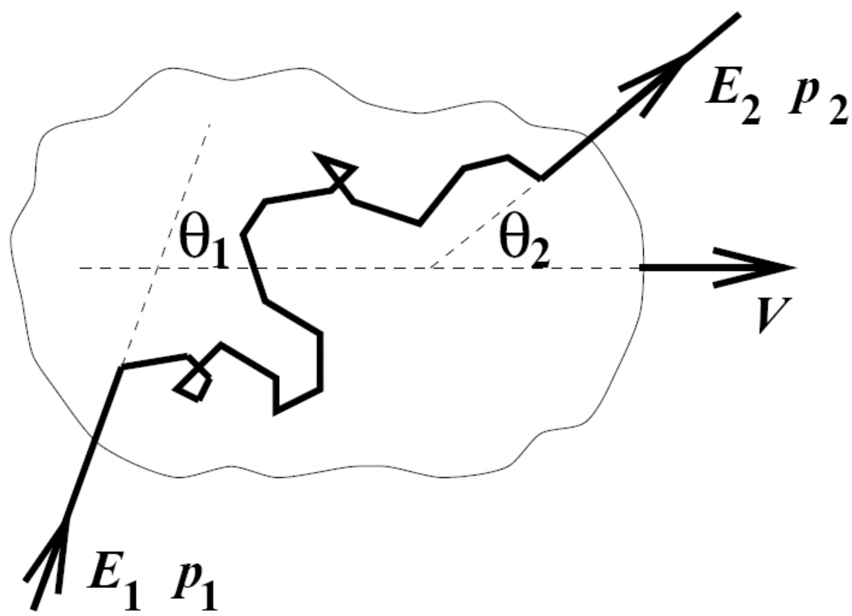

Figure 2.2: Fermi's second order acceleration. A cosmic ray particle of energy E_1, momentum p_1 enters a cloud of charged particles moving with velocity V under an angle Θ_1 wrt. the cloud velocity. After stochastic acceleration inside the cloud the particle leaves the cloud in average with greater energy E_2, momentum p_2 and under angle Θ_2. For reference see [3].

Fermi's second order theory

One of the first hypotheses how UHECR and even EHECR could gain their energy is the so called Fermi's acceleration. The first idea was presented by Fermi already in 1949. The principle lies in stochastic particle acceleration in a charged nebulae [3] which is propagating with velocity v (typically

[2]EeV is commonly used unit for energy in UHECR and corresponds to energy 10^{18} eV. For intensity of magnetic field the unit G (gauss) is used, which equals to 10^{-4} T.

[3]Under nebulae a rarefied gas of charged particles is meant.

$\sim$ 15 km·s^{-1}) and containing magnetic field B (Fig. 2.2). The particle is elastic scattered on charged irregularities contained in the nebulae. Fermi obtained that the rate of energy gain of relativistic particle of energy E and charge Ze can be written as

$$\frac{dE}{dt} = \eta Ze\, c^2 B \tag{2.3}$$

where $\eta < 1$ and depends on details of accelerating mechanism. This equation was also used by Hillas to create his well known diagram serving for first orientation to search for possible sources of EHECR (Fig. 2.3). Fermi's original theory describes averaged energy gain of charged particles traversing through cloud as

$$\frac{\Delta E}{E} \simeq \frac{4}{3}\beta^2 \tag{2.4}$$

where β is the Lorentz velocity of cloud. The derivation in a simplified way may be found in [4]. Thus, in average, the particle gains positive energy boost and it is accelerated. The particle may be accelerated by this way in many further nebulas. Since the energy gain is proportional to the second power of β this theory is called as Fermi's acceleration of the second order.

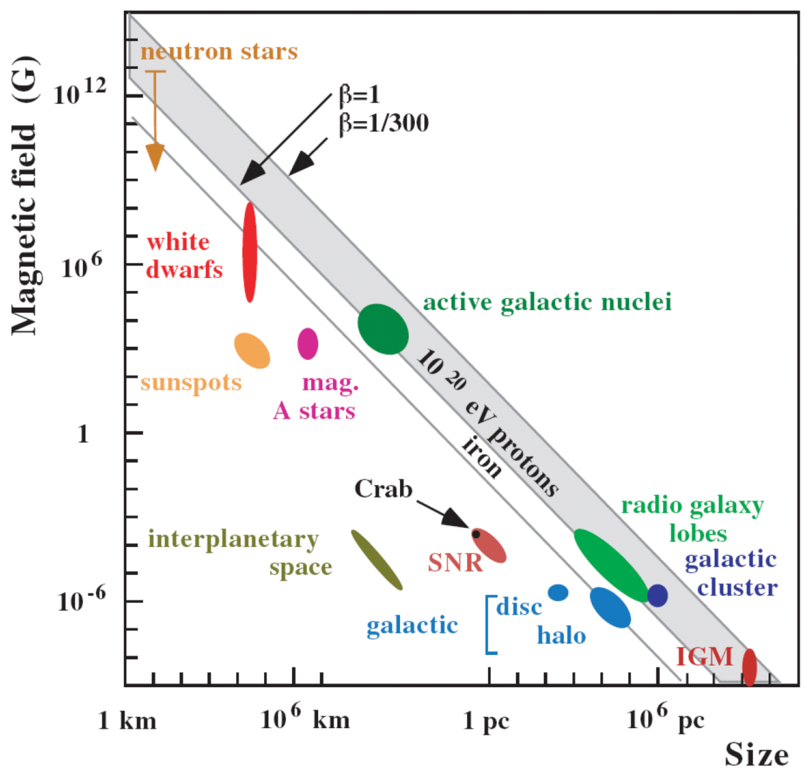

Figure 2.3: Hillas's diagram of possible EHECR sources. Cosmic objects are depicted according to their intensity of magnetic field and characteristic size along which particles may be accelerated. SNR corresponds to supernova remnants, IGM to intergalactic matter and β expresses the effectivity of accelerating process. Objects below the line are unable to reach EHECR energies in the first approximation. The position of active galactic nuclei is worth to notice. Picture comes from [5].

Fermi's first order theory

The Fermi's original theory was further developed and even theory with accelerating boost proportional only to the first order of β was achieved. The considered mechanism takes place in supernova explosions or, generally, in any other strong shocks of astrophysical environment. Particles gain their energy during circulating around the shock wave which moves in the interstellar medium with higher velocity than the speed of light in this medium. In front and behind of the shock wave the gas may be described as clouds in Fermi's original theory. Since the typical velocities of ejected material from supernovae are $\sim 10^4$ km$\cdot$s^{-1} and the energy boost depends only on the first power of β this theory is much more efficient accelerating mechanism than Fermi's second order theory.

There are many other hypotheses of EHECR origin. From the variety of "classic" cosmic accelerators the most considered sources are active galactic nuclei with jets oriented to the observer (labeled as blazars). Another theories propose relic neutrinos (energy $\gtrsim 10^{22}$ eV), decay of relic superheavy particles (lifetime greater than age of universe), dark matter particles, monopoles or violation of Lorentz invariance. A brief summary of possible UHECR sources may be found in [4].

2.4 Energy Spectrum

Very important feature of cosmic rays is their energy spectrum that may provide useful indirect information about cosmic ray origin. Markable changes in behavior of energy spectrum may signalize e.g. increase or decrease of certain type of particles participating in the spectrum or they may also uncover various processes that need certain energy threshold to arise.

The flux Φ of cosmic rays with energy E over about 10 GeV follows the dependence

$$\Phi = C \cdot E^{-\gamma} \tag{2.5}$$

where C is the normalization constant and the slope γ (denoted as spectral index) fits the majority of the spectrum for value - 2.7. The energy spectrum over 12 orders of magnitude in energy is shown in Fig. 2.4. This steep decreasing trend implies a large exposure needed for detecting UHECR corresponding to the end of the spectrum. There are three energy regions of considerable deviation in spectral index (under more detailed view when the flux is multiplied by $E^{2.7}$ in Fig. 2.5). Since the spectrum shape is usually symbolized as human leg from sideview, the region around about $10^{15.5}$ eV is known as knee (γ grows to ~ 3) and the region around $10^{18.8}$ eV as ankle (γ falls back to ~ 2.7). The third region violating the spectrum trend occurs between knee and ankle ($10^{17.8}$ eV) and is denoted as second knee (γ slightly greater than 3).

The origin of knee is mostly assigned to the fact that the accelerating regions in our Galaxy are unable to maintain protons (or lighter nuclei) inside them for further accelerations. Proton trajectories are less curved due to the increase of Larmor radius (2.2) after reaching sufficient energy and thus they escape from these regions which implies the decrease of their flux at the knee energies. Heavier nuclei are maintained longer within accelerating regions and therefore they obtain also greater energy boost. In the end even heavier nuclei escape from accelerating regions which is probably responsible for the origin of the second knee. In this way the galactic sources are gradually vanishing and the extragalactic component becomes more relevant which is mostly taken as the reason for the emergence of an ankle in the spectrum.

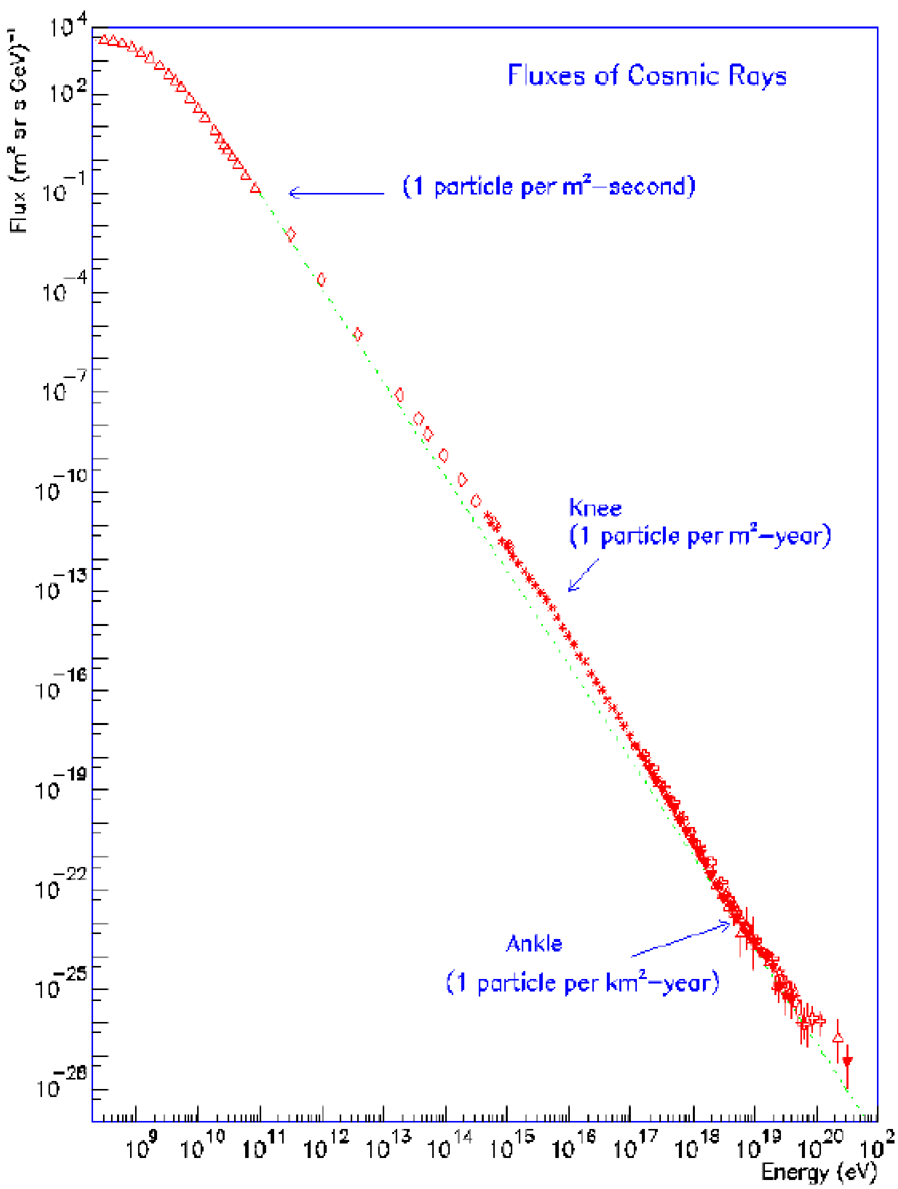

Figure 2.4: Energy spectrum of cosmic rays above 100 MeV. Two regions deviating the drawn dependence (E^{-3}) are denoted with their fluxes. Picture is taken from [6] and it is a compilation of results from LEAP, Proton, Akeno, AGASA, Fly's Eye, Haverah Park and Yakutsk experiments.

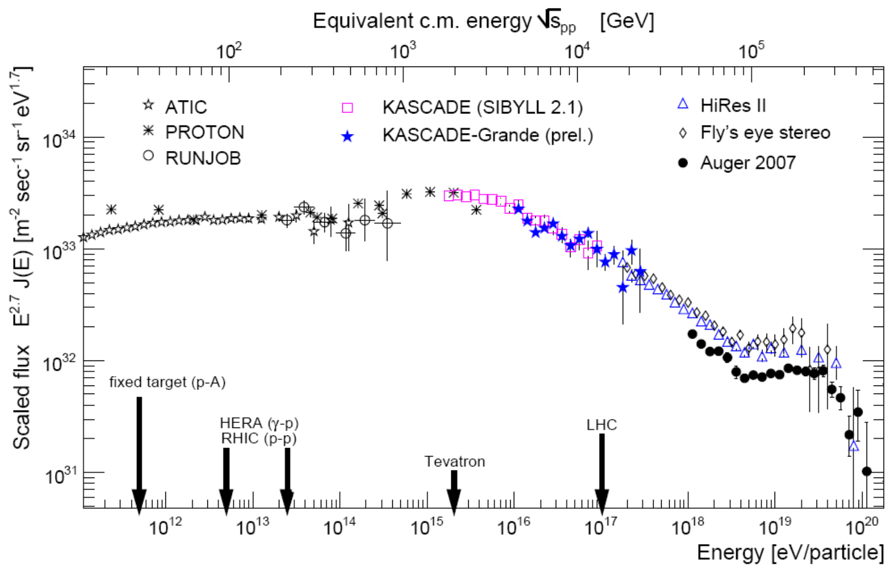

Figure 2.5: Cosmic ray energy spectrum multiplied by $E^{2.7}$ as it was measured by indicated experiments. Capability of some accelerators is also depicted for comparison. Similarity of spectrum behaviour with shape of human leg is visible. Picture is obtained from [2].

2.4.1 GZK Cut-off

First theoretical prediction about the end of the spectrum appeared already in 1966 when one year after the discovery of cosmic microwave background radiation (CMBR) [4] Greisen and independently Zatsepin with Kuzmin predicted a limit in the energy spectrum over $6{\cdot}10^{19}$ eV (so called GZK cut-off). Their prediction was based on interaction of proton with CMBR producing pions:

$$p + \gamma_{2,7K} \rightarrow n + \pi^{+}\,, \tag{2.6}$$

$$p + \gamma_{2,7K} \rightarrow p + \pi^{0} \tag{2.7}$$

with energy threshold $6 \cdot 10^{19}$ eV of impingning proton. Another competitive process considered is the pair production:

$$p + \gamma_{2,7K} \rightarrow p + e^{+} + e^{-} \tag{2.8}$$

which has much smaller energy threshold, however, also much smaller energy losses. Despite the fact that this process has 6-times shorter mean free path, the dominant process for propagation of EHECR is the pion production due to greater energy losses. The comparison of these two competive processes is shown in Tab. 2.1. With energy greater than 10^{20} eV the cross section of pion production grows up and thus protons reaching Earth from distance greater than 100 Mpc should not exceed the energy 10^{20} eV as it is shown in Fig. 2.6.

[4]CMBR fills up the cosmic space with density about 400 cm^{-3} and temperature 2.7 K, which corresponds to the mean energy $6{\cdot}10^{-4}$ eV.

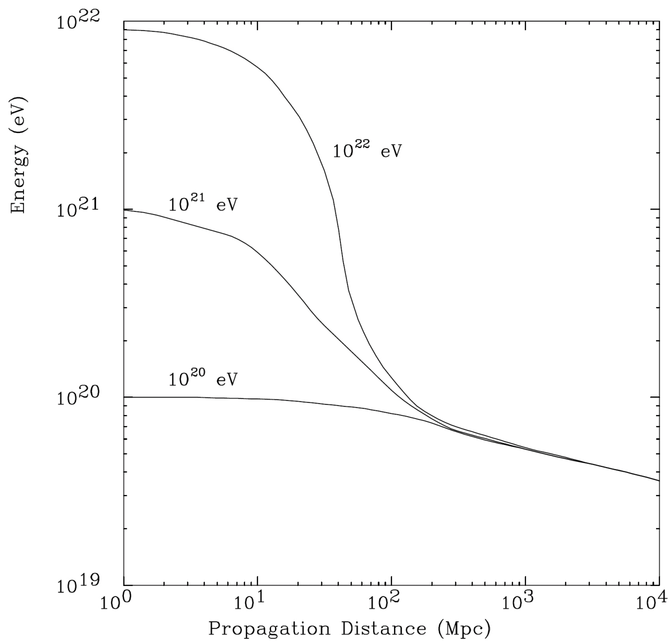

Figure 2.6: Mean energy as a function of propagation distance for protons with three different original energies. Picture is taken from [7].

Production	E_{Th} [eV]	$\frac{\Delta E}{E}$ [%]	l [Mpc]
$\pi^{\pm,0}$	$10^{19.6}$	20.0	6
$e^+ + e-$	$10^{18.0}$	0.1	1

Table 2.1: Comparison of competitive processes in propagation of UHECR proton through extragalactic space. Threshold energy (E_{Th}), energy losses ($\frac{\Delta E}{E}$) and mean free path (l) are obtained from [8].

Analogous cut-off was calculated also for nuclei with mass number A proceeding photo-disintegration processes:

$$A + \gamma_{2,7K} \rightarrow (A - 1) + N\,, \tag{2.9}$$

$$A + \gamma_{2,7K} \rightarrow (A - 2) + 2N \tag{2.10}$$

and pair production:

$$A + \gamma_{2,7K} \rightarrow A + e^+ + e^- \tag{2.11}$$

where N denotes proton or neutron. The energy-loss rate for two-nucleons emission is about one order of magnitude lower than for one-nucleon emission. The most notable effect of pair production to the rate of energy losses is in the energy region between $5 \cdot 10^{19}$ eV and $2 \cdot 10^{20}$ eV. The calculated attenuation length [5] of iron, proton and gamma-photons is depicted in Fig. 2.7.

[5] On the contrary to mean free path (mean distance before interactions) the attenuation length is the distance after which the particle energy E has decreased to $\frac{E}{e}$.

For gamma rays the pair production in interaction with CMBR:

$$\gamma + \gamma_{2,7K} \rightarrow e^{+} + e^{-} \tag{2.12}$$

is the most important process in wide energy range above the threshold $4{\cdot}10^{14}$ eV. At the end, for energies above $2{\cdot}10^{19}$ eV the creation of electron-positron pairs by interaction with radio-background photons from radio galaxies becomes dominant. It follows from Fig. 2.7 that below EHECR energies it is expected to detect minimum of photon-induced showers which would contain very small number of muons. On the other hand the theoretically predicted growth of attenuation length for photons of energy greater than 10^{20} eV increases the probability of detecting EHECR photon. Despite this fact, it would have to be produced much closer to Earth in comparison with proton and iron of the same energy. No UHECR shower was yet clearly identified as photon-induced and therefore only various upper limits for UHECR photon flux are estimated.

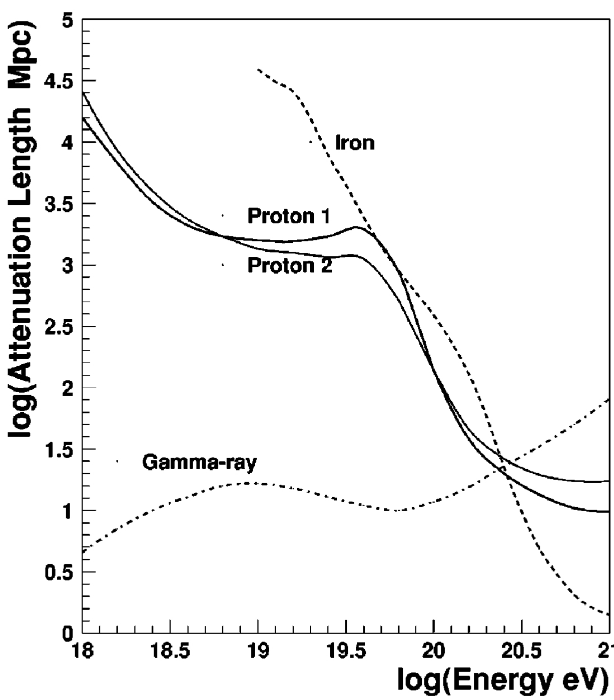

Figure 2.7: The attenuation length of proton, iron and gamma-ray primaries in the microwave, infrared and radio background as a function of energy. Picture is taken from [8].

2.4.2 Conflicting Observations of GZK before PAO

The AGASA (Akeno Giant Air-Shower Array) experiment did not observed the expected steep decrease of cosmic ray flux above $6 \cdot 10^{19}$ eV on the contrary (Fig. 2.8) to data of the HiRes experiment (High Resolution Fly's Eye). Thus one of the strongest motivations for building of PAO was to justify results of these two experiments. AGASA used field of surface detectors with energy calibration relied on simulations while HiRes was a fluorescence detector which was calibrated with lesser dependence on simulations. Comparison of these contradictory results with the PAO data is described in the next chapter.

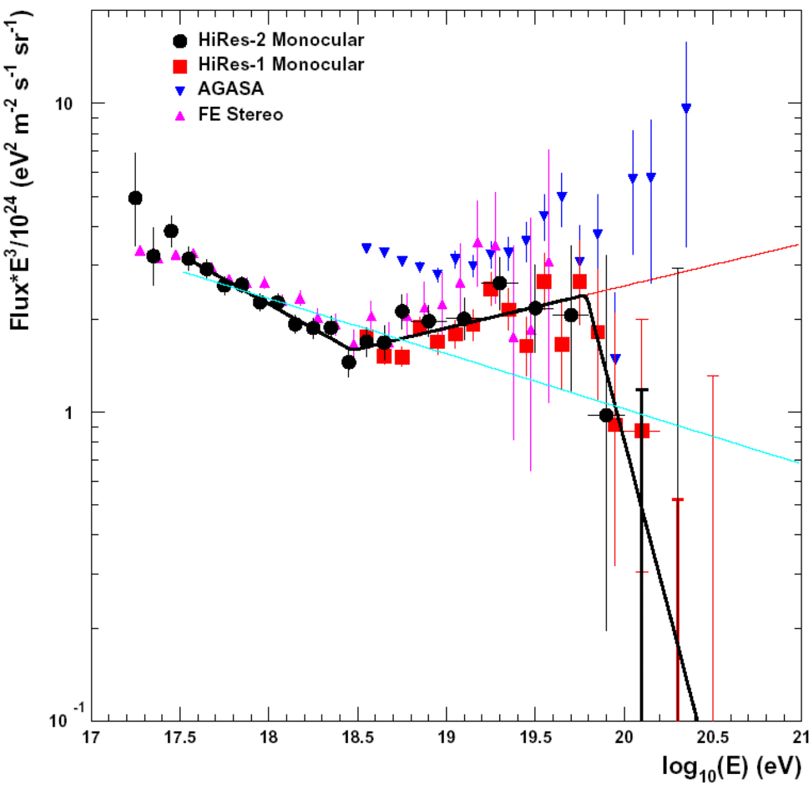

Figure 2.8: Energy spectrum inferred by AGASA and HiRes. Data from AGASA do not confirm the GZK cut-off assumption on the contrary to flux measured at HiRes which steeply decreases above the threshold energy for pion production. Data from experiment Fly's Eye, which was the precursor of HiRes, are also shown. For reference see [9].

Chapter 3

The Pierre Auger Observatory under Magnifying Glass

The development of giant detection fields studying UHECR proceeded great progress during operation of many experiments in last 50 years [1]. Individual experiments of the greatest importance may be found in [8]. The culmination of this development is just the present project Pierre Auger Observatory (PAO).

To cover full sky exposure, PAO was divided into two parts. The first of them was completed in autumn 2008 and it is built on the southern hemisphere - in Argentinean province Mendoza, near the city of Malargüe. The second part of Observatory is planed to be built in the northern hemisphere - on the Colorado's plains in USA. It was decided to build the southern observatory first, since there were some speculations about EHECR origin in the center of our Galaxy that is located in the constellation Sculptor which position is sufficiently high on the sky for observation only on the southern hemisphere [2].

The PAO is the largest experiment for studying UHECR ever built. The main objective of the project is to detect cosmic ray particles of energy higher than $\sim 10^{18}$ eV, especially it is aimed for 100 % efficient detection of EHECR. Moreover the sub-project AMIGA (Auger Muons and Infill for the Ground Array) is setting up at the present time, which will move the lower energy threshold of the Observatory to about $3 \cdot 10^{17}$ eV. It will permit to observe the flux around the second knee region.

The PAO is extended over an area of 3 000 km^2 on Argentinean plain at altitude about 1 400 m a.s.l. The field of more than 1 600 tanks of water Cherenkov detectors forms the giant Surface Detector (SD), which offers a large SD exposure [3] for measurement. Fluorescence Detector (FD) buildings are installed around this field at 4 hills (Fig. 3.1) and provide another independent type of shower de-

[1] The experiment Volcano Ranch in New Mexico is considered as the first giant array. It started to be operational already in 1961.

[2] In the following text the finished southern part of the project Pierre Auger Observatory is considered under the abbreviation PAO.

[3] The SD exposure of PAO was estimated to $\sim$ 22 300 km$^2\cdot$ s$\cdot$ y at 1. 3. 2010. This was approximately 14 times larger than the total exposure of so far largest experiment AGASA which used surface detector array of plastic scintillators.

tection. Connecting FD with SD measurement the so called hybrid detection technique is performed. The PAO is operated in its designed size since autumn 2008, however the science data-taking was possible since the end of 2003 with smaller array.

Due to hybrid reconstruction of events the PAO reaches so precise measurements that conclusions about energy spectrum, mass composition and anisotropy may be assumed with precision markedly overtopping previous experiments dealt with UHECR. Another remarkable step in evolution of UHECR detection used at the PAO is the energy calibration of surface detector field using hybrid detected events. This calibration is almost independent of simulations on the contrary to previous experiments where the energy calibration relied on results from simulations much more.

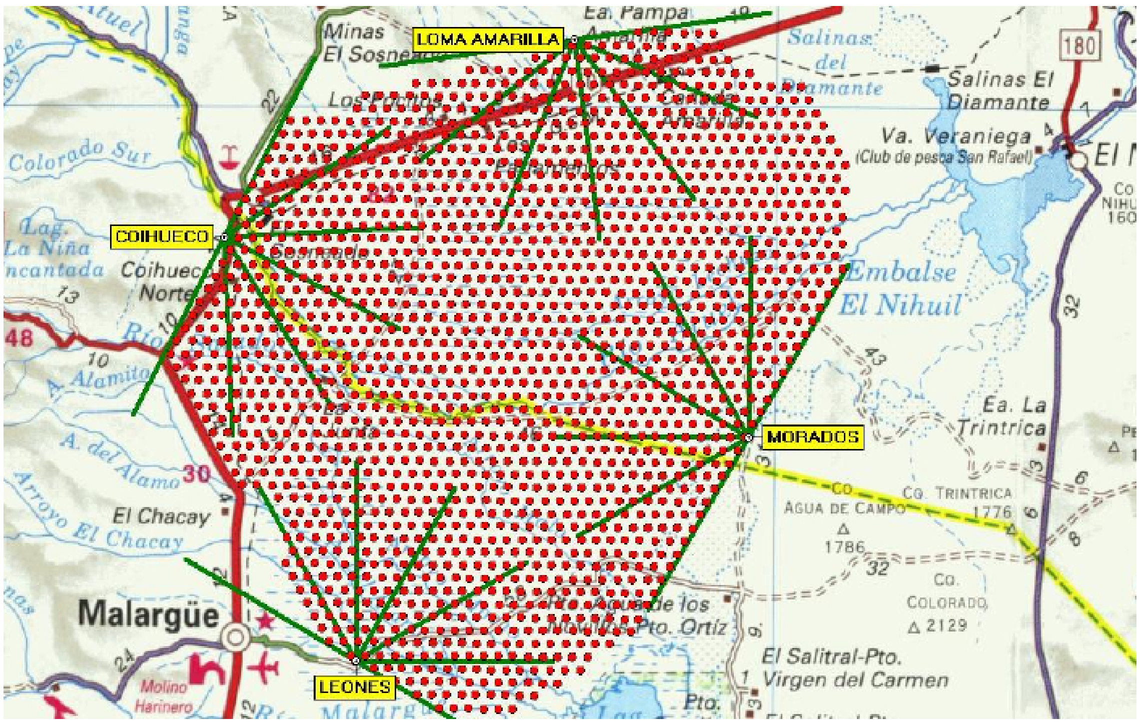

Figure 3.1: The view of the PAO experiment. Red spots are representing tanks of the surface detector array, yellow labels are the names of 4 hills on which 4 fluorescence detectors are installed. The green lines demonstrate schematically the azimuthal field of view of the individual fluorescence telescopes. Picture comes from [7].

3.1 Surface Detector Field

Cylindrical tank of water forms the individual units of the surface detector field. 12 000 l of high purified water, which is used as the Cherenkov radiator medium, are filled into a polyethylene cylinder (Tyvek Liner) of diameter 3.6 m and height 1.55 m. The Cherenkov light is produced when charged particles with velocity greater than speed of light in water traverse through the detector. The Cherenkov photons are reflected by the liner and they are collected by 3 photomultiplier tubes (PMTs) located in the roof of the detector as it is schematically drawn in Fig. 3.2. Each photomultiplier has semispherical collecting surface of diameter 9" ($\sim$ 23 cm). The digitalized signal from PMTs is operated by local CPU. Time information is provided by GPS Motorola unit and all the electronics is powered by two 12 V batteries charged by solar panels. Signals satisfying local trigger conditions are sent to the Central Data Acquisition Station (CDAS) for testing physical triggers. Each SD unit is an independent detector and it was able to take data soon after its installation. This enabled the PAO to take scientific data during whole SD installation process.

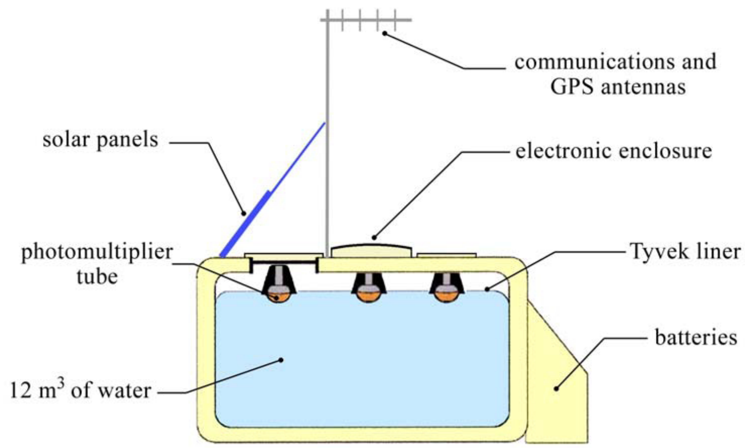

Figure 3.2: Description of water Cherenkov detector used at the PAO. Cross section of cylindrical tank with accessories is depicted. Picture is obtained from [10].

All 1 600 Cherenkov detectors are alined into a regular triangular grid with spacing of 1 500 m. This setting is crucial for decision which shower energy range is measured. The spacing of SD field was chosen to optimise financial demand together with maintaining sufficient number of triggered tanks for reconstruction of detected UHECR showers [4].

A Shower detected by SD is seen as a sequence of various time-spatial signals. After successfull reconstruction used by Offline algorithm the most important shower characteristics are the location of shower axis, position of shower core and the lateral distribution function (LDF). The LDF is a fitted function describing the decrease of the SD signal with distance to shower core in the plane perpendicular to the shower axis. The so called NKG [5] function is used for LDF form at the PAO:

$$S(r) = S(r_0) \cdot \left(\frac{r}{r_0}\right)^{-\beta} \left(\frac{r + r_s}{r_0 + r_s}\right)^{-\beta} \tag{3.1}$$

where S is the predicted signal in the distance (r) from shower axis, β the slope parameter, r_s was set to 700 m and r_0 was chosen to 1 000 m as it is explained in the following subsection.

[4]The experiment SUGAR near Sydney, the only UHECR experiment placed on the southern hemisphere before the PAO, used array spacing of 1 mile (1609 m). Showers were mostly detected by only few stations and thus their reconstruction suffered by large errors, which caused their impropriety for further scientific analysis.

[5]Named after Nishimura, Kamata and Greisen (1956).

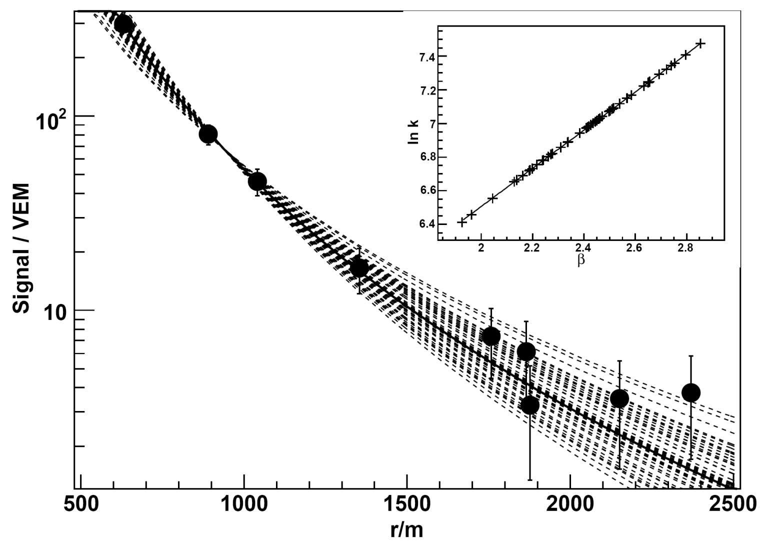

Figure 3.3: The same simulated event 50 times reconstructed for different values of the slope parameter β of the LDF. The NKG form of the LDF is used. The inset plot shows the relationship between the slope parameter β and the fitted size parameter k, which is $S(r_0)$, allowing r_{opt} to be calculated analytically. The unit of the signal is VEM, which is the signal produced by muon of energy 250 MeV vertically penetrating the surface detector. For reference see [11].

3.1.1 Optimal SD Parameters for Energy Conversion

The reconstructed LDF signal depends, besides on the distance from shower core, mainly on shower energy and also on zenith angle. Thus, at first, it is needed to introduce for all events some conventional distance from the shower axis at which the LDF is converted to shower energy.

Fig. 3.3 plots the signals of individual water Cherenkov detectors in case of a given simulated event as a function of their distance to shower core. The signals are fitted by equation (3.1) for different slope parameters β. The reasonable range of β parameter is obtained by the error assigned to it, if the β parameter is allowed to be free in the fit. It follows from the figure that there is a distance around 1 000 m where the size of fluctuations given by different fits is minimal. Optimal distances of the similar sizes can be obtained for all events although they are somewhat depending on the particular event chosen. It was shown in [11] that the typical size of optimal distance depends on the spacing of the nearby detectors as it is illustrated in Fig. 3.4.

For PAO with SD arranged into the triangular grid with spacing 1 500 m the optimal distance r_{opt} is close to 1 000 m for different events. Thus the LDF at 1 km ($S1000$) is a good choice for further energy conversion with minimum fluctuations emerging from the uncertainty of the fitted LDF.

The signal $S1000$ is also dependent on the zenith angle of shower axis. This dependence is called the attenuation curve and is obtained applying the Constant Intensity Cut method as it will be explained in the next chapter. For the conversion of $S1000$ to energy of the shower another reference value (independent on zenith angle) is therefore needed. The reference value ($S38$) was chosen as the

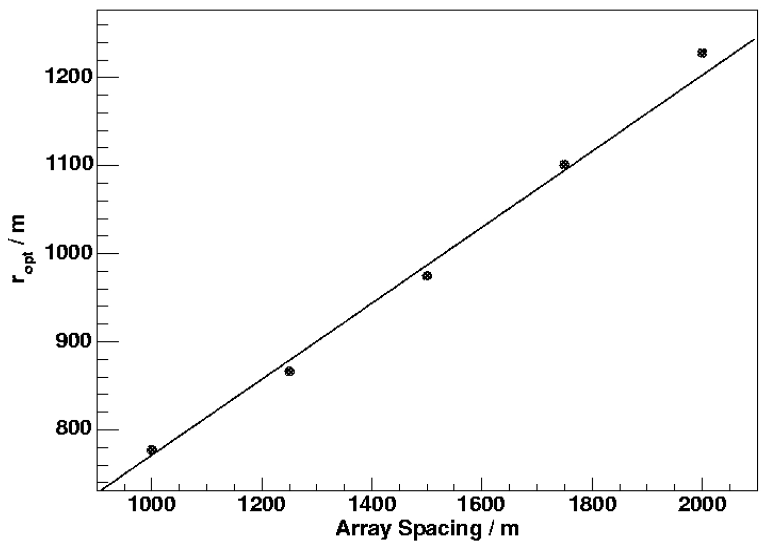

Figure 3.4: The dependence of the optimal ground parameter r_{opt} on the array spacing. The SD array with regular triangular grid is considered. For PAO with spacing 1 500 m the optimal parameter of value 1 000 m seems to be a good choice for conversion of the LDF to energy. Picture comes from [11].

$S1000$ signal of the same shower if it would arrive with zenith angle 38°. This angle was chosen since the angular distribution for energies above 3 EeV reaches median at this value.

Relative timing information from N individual activated tanks (N-fold event) allow to reconstruct the axis of the shower of energy E from fitting procedure with angular accuracy better than 2.2° for 3-fold events ($E < 4$ EeV), better than 1.5° for 4-fold and 5-fold events (3 EeV $< E <$ 10 EeV) and for events with higher multiplicity ($E >$ 10 EeV) even better than 1°according to [12].

3.1.2 SD Trigger System

SD trigger system was created to provide shower detection in wide energy range and also to be fully efficient for EHECR. Two local trigger levels are processed by local CPU at individual tanks. Higher trigger levels are controlled at CDAS. The first level trigger T1 contains two modes (ToT and T1 threshold).

ToT: The first mode of T1 trigger, Time over Threshold (ToT), demands two coincident current collection from PMTs. At least in 13 from 120 channels (3 μs window) the current impulses have to be higher than 0.2 I^{est}_{VEM}. The unit I^{est}_{VEM} corresponds to the expected current signal of vertically penetrating muon of energy 250 MeV. ToT is of small rate (1.6 Hz) but it may recognise shower signals in greater distances from shower core or less energetic showers.

T1 threshold: Another part of T1 transmits only events of three-PMT coincidence signals containing at least 3 channels of signal greater than 1.5 I^{est}_{VEM}. This trigger is more disturb by background (rate $\sim$ 100 Hz) but it permits to detect muon component of horizontal showers [6].

T2: The second level trigger (T2) attends to choose shower signals from background and to reduce the rate to value 20 Hz, which is the frequence of individual tank data signals sent to CDAS. All ToT are automatically promoted to T2 but the other data has to fulfil the condition demanding three-PMT detection coincidence of signals exceeding 3.2 I^{est}_{VEM}.

T3: The third level trigger (T3) is processed at CDAS and contains also 2 modes. The first of them (3ToT) requires coincidence of three tanks with ToT and a condition of a little compactness (at least one tank has to be surrounded by one active tank of its closest and one of the second closest neighbour tanks). 3ToT is a very important trigger since 90 % of such triggered data belongs to physical showers. The second part of T3 is of low rate and small efficiency of physical showers ($\sim$ 2%) but it is crucial important for detection of horizontal showers. It requires four T2 triggered tanks in coincidence satisfying a condition of moderate compactness (none of 4 active tanks is allowed to be distanced far from 3 others tanks more than 6 km).

T4: The T4 trigger is known as physical trigger that mainly ensures high probability of real (physical) shower detection and reduces random coincidences. It has also, as previous three trigger levels, one mode aimed to showers up to zenith angle of 60° and one mode of low rate devoted to horizontal showers. The former applies the so called compact 3ToT (3ToTC1) condition. This compactness demands at least 3ToT to form a triangle of first neighbours. Requiring this compact condition 99 % of detected showers with zenith angle less than 60° are physical showers but about 5 % of showers remains undetected. To reduce the latter number and also to detect inclined showers the second mode is used. It is required that at least one active tank has 3 active surrounding tanks out of its 6 closest neighbours. The trigger times are also compared to satisfy shower propagation with speed of light. Isolated stations are removed from further shower reconstruction.

T5: This quality trigger is used to ensure that no information necessary for shower reconstruction is missed. T5 requires that the station with highest signal is surrounded by at least 5 active tanks of its 6 nearest neighbour stations (Fig. 3.5). This condition guarantee that the shower core is located inside the SD aperture and also that sufficient number of tank signals is sampled for good reconstruction.

3.2 Fluorescence Measurement

Besides SD detection of extended showers the PAO uses also the fluorescence detection technique which is much younger and also more complex than the measurement using array of surface detec-

[6] Showers with zenith angle from range (60°, 80°) are denoted as horizontal showers

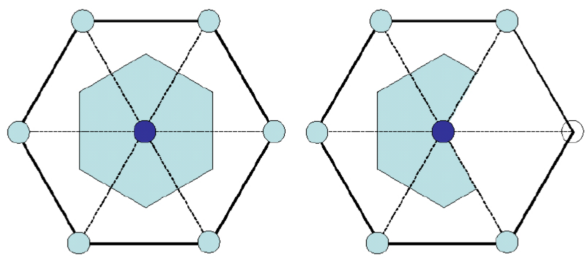

Figure 3.5: Quality T5 trigger used in SD detection. Picture is comes from [13].

tors. During the shower development nitrogen molecules in the atmosphere are excited by charged secondary particles and by their consecutive deexcitation fluorescence photons (300 - 430 nm) are emitted. They are collected by fluorescence telescopes together with contamination of produced Cherenkov photons and sky light background. This type of detection was previously used by experiments Fly's Eye and HiRes and nowadays besides PAO fluorescence telescopes are installed also in the experiment Telescope Array which is currently under construction.

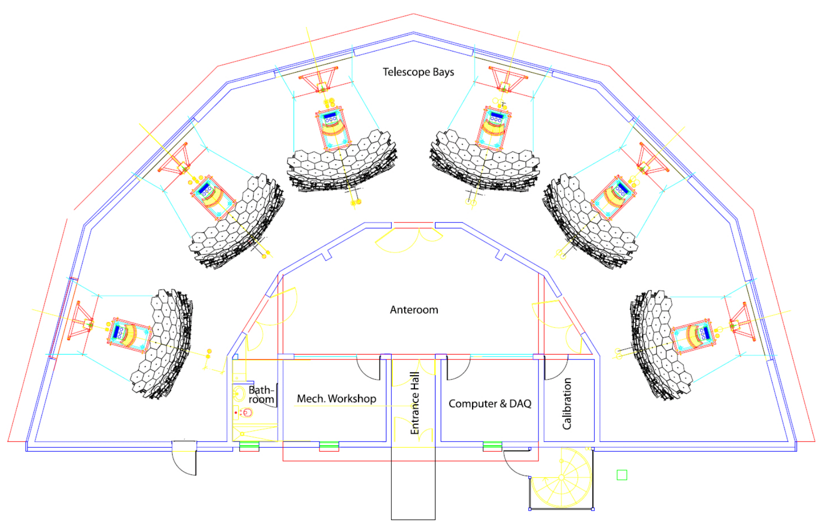

Figure 3.6: Schematic view of a fluorescence detector building with 6 bays containing fluorescence telescopes. Picture is taken from [14].

3.2.1 Fluorescence Detector

One fluorescence detector building at the PAO (Fig. 3.6) consists of 6 fluorescence telescopes. Each telescope (Fig. 3.7) is located in the so called bay and gathers the light 30° in azimuthal and 28.6° in vertical direction. A spherical mirror of curvature 3.4 m and surface 13 m^2 focuses the light on the field of 440 photomultiplier tubes (PMTs). Each photomultiplier pixel of hexagonal shape fills the view angle of about $1.5° \times 1.5°$. The used Schmidt optical system with corrector ring enhances the telescope aperture by factor of ~ 2. UV filter is also installed in this aperture system. The telescope mirror is divided into 36 rectangular (Los Leones, Los Morados) or 60 hexagonal (Coihueco, Loma Amarilla) mirror segments for simplification of manufacturing and for reduction of the telescope cost.

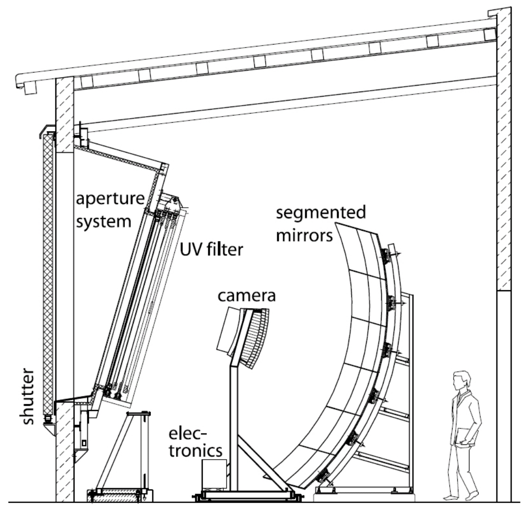

Figure 3.7: Schematic view of a fluorescence telescope with major parts of the instrument described. Picture is obtained from [14].

The FD telescopes are able to measure almost only during moonless nights. They are very sensitive since they have to collect small fluorescence signals and even background light from brightest stars has to be taken under consideration in data taking. Thus it is needed to protect PMTs from the strong light background mainly from sunshine and moonlight. This is solved by closing the telescope shutters and lowering the voltages when the light background exceeds certain level. Therefore FD measures in duty cycle about 13 % of the total time on the contrary to SD which is able to measure almost 100 % of the time.

3.2.2 Energy Conversion

Isotropic emissions of fluorescence photons (on the contrary to forwarded Cherenkov photons) guarantee that the longitudinal shower profile may be detected from distant locations. Besides this isotropic feature it is also important for conversion of the signal to energy, that the intensity of the detected FD signal is proportional to the number of charged secondary particles and thus also to the deposited shower energy. Showers of the same energy with different zenith angles produce the same intensity of fluorescence light assuming they propagated up to the same atmospheric slant depth X [7], which allows general conversion of fluorescence light intensity to energy for all showers.

The fluorescence detector determines the longitudinal shower development profile $\frac{dE}{dX}(X)$, which describes the energy deposited in the atmosphere by electromagnetic component. An example of

[7] Similarly as for the X_{max} definition, the atmospheric slant depth corresponds to the atmospheric mass through which the primary particle would have to penetrate.

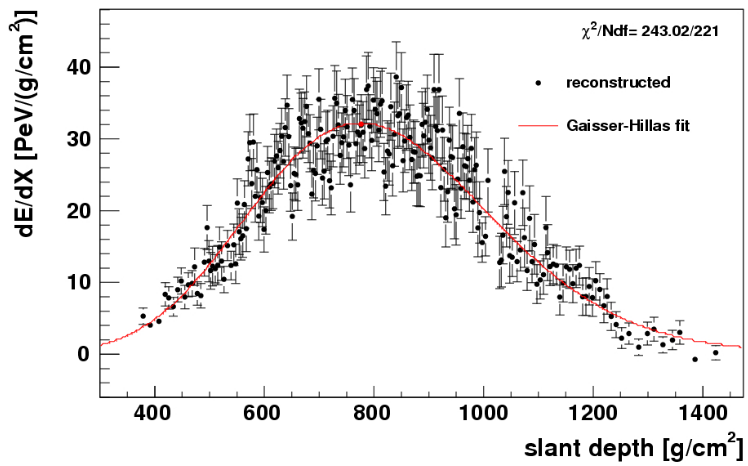

Figure 3.8: Typical shower longitudinal profile of EHECR event measured at the PAO by FD. The profile is fitted by the Gaisser-Hillas fit with Auger Offline which is a tool for reconstruction of events.

measured profile together with used Gaisser-Hillas fit is shown in Fig. 3.8. Integration of this profile (from zero to infinity) provides total energy dissipated electromagnetically, which is approximately 90 % of the total primary particle energy according to simulations. The remaining energy portion is formed mainly by muons and neutrinos. To be able to convert the detected signal ($\sim$ number of fluorescence photons) to the longitudinal profile it is needed to know air density as a function of altitude and the fluorescence yield. The latter quantity is defined as number of photons in a given fluorescence wavelength band emitted per unit of energy deposited in the atmosphere by charged particles [8].

3.2.3 FD Trigger

As for SD the FD trigger is also hierarchically ordered. It starts from individual pixels and the highest level trigger allows even to evoke additional SD data for hybrid detection.

FLT: The main first level trigger (FLT) function is built to decide if the integrated signal of a single pixel in the time window exceeds a certain threshold and then this pixel is marked as active. The threshold is dynamically adjusted to maintain pixel trigger rate of 100 Hz. Further function of FLT is to store background data and multiplicity of pixels for experimental control.

SLT: The second level trigger (SLT) searches for patterns (Fig. 3.9) in the field of hexagonal pixels (22×20). To prevent situations when two neighbour photomultipliers collect light from shower but the signals are not enough strong to pass FLT, only 4 pixels are required to be active from 5 pixel patterns.

[8] The absolute fluorescence yield of wavelength 337 nm, as it was measured in [15], is 5.05 ± 0.71 photons per 1 MeV of deposited energy in air of temperature 293 K and 1013 hPa.

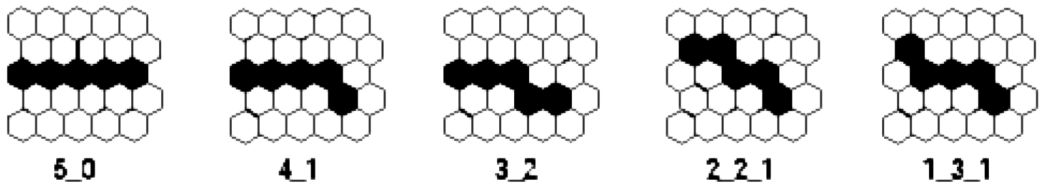

Figure 3.9: Fundamental 5-fold pixel patterns used in SLT of FD. Requiring only 4 from 5 pixels to be activated 108 patterns (including pattern rotations and mirroring) at all has to be checked within field of 22×20 pixels during every 1 μs. Picture comes from [7].

TLT: The third level trigger (TLT) is a software designed to distinguish cosmic ray showers from lightnings, randomly triggered pixels and from muons passing through the field of photomultipliers. After studying shower detection in the first year of Observatory operation a requirement for removing events containing more than 25 active pixels was applied, which removes lightning events with 99 % probability. To discard randomly activated pixels or pixels triggered far from light track by penetrating muons a correlation of spatial arrangement and peak signal times is applied. From simulations and measured data it is assumed that 94 % of background events is removed and the fraction of true shower rejected by TLT is below 0.7 %.

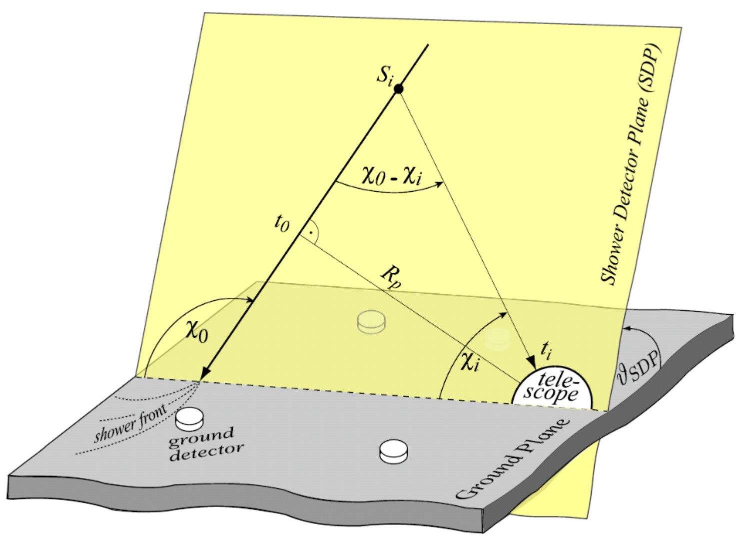

Figure 3.10: Illustration of geometrical reconstruction by fluorescence detection at the PAO. Observables used in the reconstruction are described. Parameters R_p and χ_0 unambiguously determine the shower axis. Picture is taken from [16].

3.2.4 FD Reconstruction

The highest fluorescence signal origins near the shower axis. Thus, after using the appropriate trigger, the shower axis is viewed as the path in the field of hexagonal pixels (Fig. 3.12). The shower energy is proportional to the signal of active pixels integrated over the path in the pixel field. Given the fluorescence yield the total signal can be directly converted to the shower energy.

The shower detection plane, defined in Fig. 3.10, is reconstructed from activated pixels in fluorescence detector. Fitting procedure which uses individual pixel timing information allows to determine the shower axis. Following function is used to fit shower axis:

$$t_i = T_0 + \frac{R_p}{c} tan[(\chi_0 - \chi_i)/2] \tag{3.2}$$

where time of pixel activation t_i and pixel angle χ_i are fitted with χ^2 technique to determine three parameters (T_0, R_p and χ_0). Time T_0 corresponds to the moment when the shower front intersects the point of shower axis with minimal distance R_p to the FD. Angle χ_0 equals to $\pi - \phi$ where ϕ is the zenith angle of the shower axis.

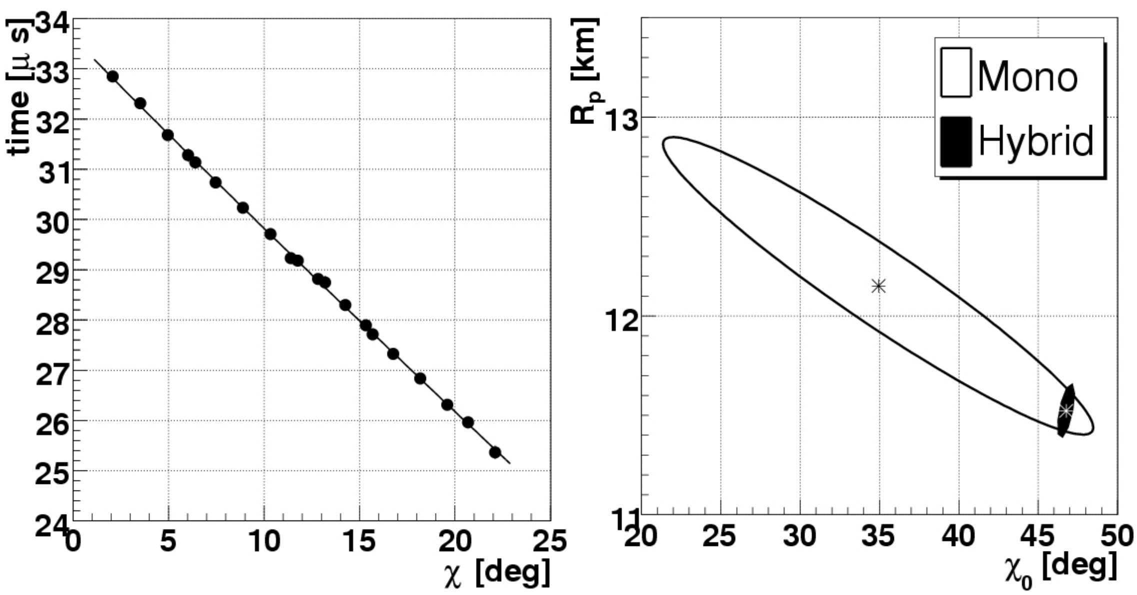

Figure 3.11: **Left:** Fitted time dependence on angle χ of individual active pixels by FD shower detection for one selected event. The fitted line depends on 3 parameters (R_p, χ_0 and T_0). **Right:** Illustration of parameter errors due to fitting procedure (3.2). Remarkable improvement of results using time information (T_0) from 7 active tanks of SD is highlighted. For reference see [17].

3.3 Hybrid Detection

The most important characteristic of the PAO experiment is the first continual usage of the so called hybrid detection when the same shower is detected by surface and fluorescence detector simultaneously. A typical EHECR event detected by the PAO hybrid technique is schematically shown in Fig. 3.12. With this type of observation it is possible to achieve very high accuracy of the primary particle direction. Even more important aspect of the hybrid detection is the energy calibration of SD measurements by FD data as it is described in details in the next chapter.

The principle of hybrid detection lies in the supplement of equation (3.2) by timing information (T_0) from SD measurement. Time information of the shower's arrival obtained even by only one tank improves the FD measurement significantly. In Fig. 3.11 this improvement is shown.

3.3.1 Hybrid Trigger

The TLT of FD is also a subsequent trigger for SD. It automatically triggers SD data and searches for active tanks that may provide time information for FD measurement. This trigger is very important for showers below energy threshold $3{\cdot}10^{18}$ eV where the SD trigger is not fully efficient. It automatically searches for individual active tanks that occur within 20 km (approximately one-quarter of the SD array) from the FD. That way it may evoke SD data which did not pass SD trigger and without hybrid trigger they would be lost. Showers of energy below $3{\cdot}10^{18}$ eV often activate only one or two tanks, which is not enough large number of tanks to activate T3 of SD.

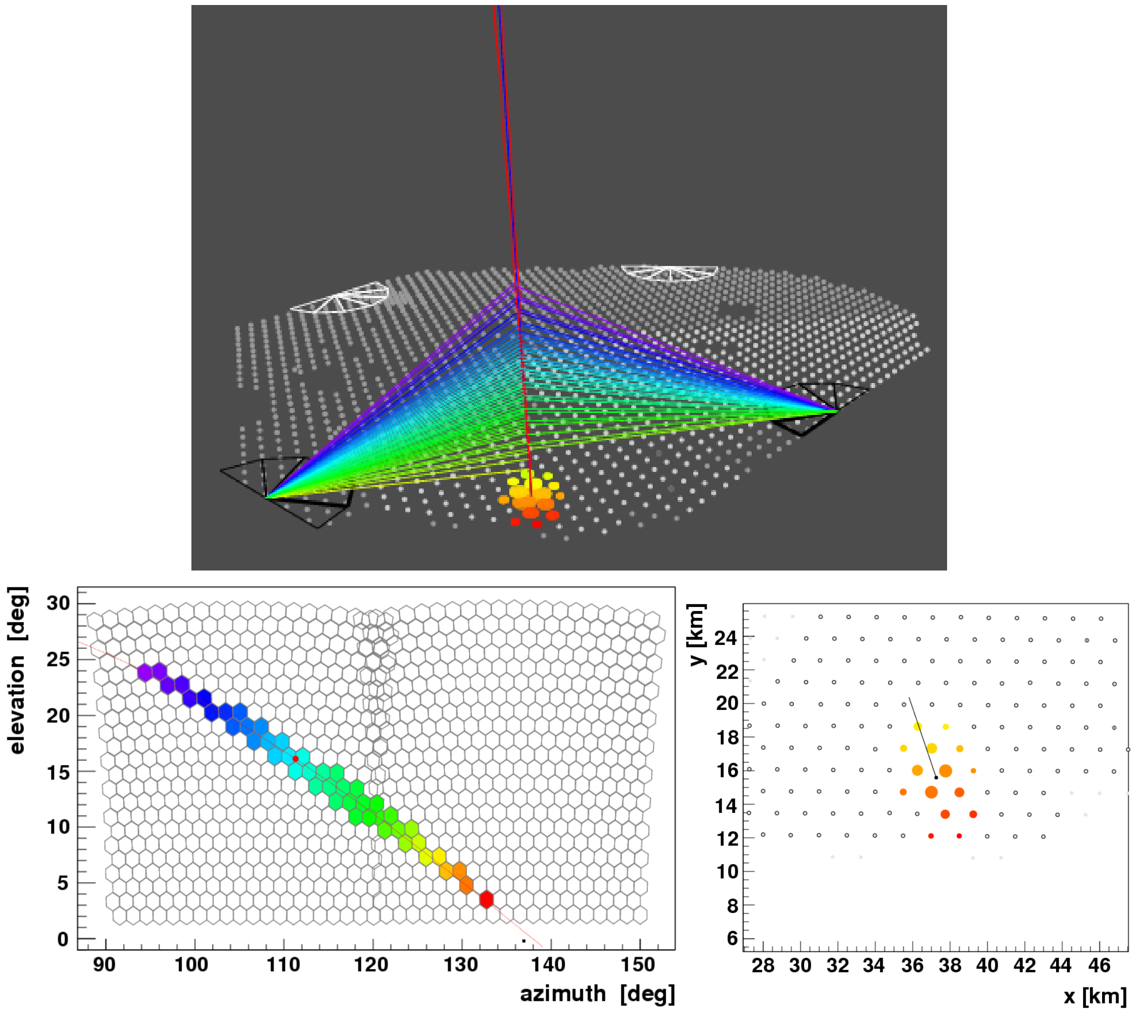

Figure 3.12: Typical EHECR shower detected at the PAO simultaneously by two fluorescence detectors and by SD field. In all pictures the detection time sequence is distinguished by colour. **Top:** Schematic draw of reconstructed shower axes together with lines describing detection of individual illuminated pixels used for FD reconstructions. SD field and 4 FDs are also depicted in a symbolic way. **Lower left:** Reconstructed shower path in the pixel field of two fluorescence telescopes is drawn as it is seen by fluorescence detector. The position of X_{max} is marked with red spot. **Lower right:** Activated tanks in the SD field are drawn with various size of circle according to the induced height of tank signal. The direction of reconstructed shower axis is showed. Pictures were created in Auger Observer tool.

3.4 Selected Results of the PAO

A brief description of some physics results obtained so far by the PAO are presented in this section.

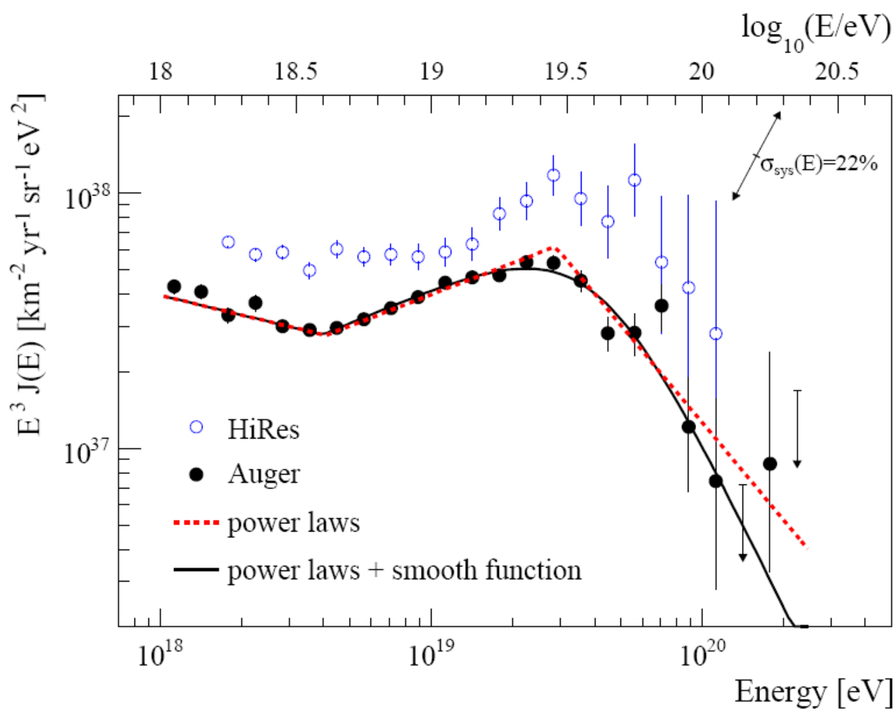

Figure 3.13: Flux of UHECR multiplied by E^3 for experiments HiRes and PAO. The combined spectrum (SD and Hybrid data together) of PAO is fitted by two functions describing characteristic feature of the spectrum. Estimated systematic error due to uncertainty of the energy scale is indicated by arrows. Picture is obtained from [18].

3.4.1 Flux at the End of Energy Spectrum

As it was indicated in section 2.4.2, one of the PAO main goals was to justify the differencies in the flux behaviour at the end of the energy spectrum measured by previous experiments AGASA and HiRes. The PAO data indicates (Fig. 3.13) steep decrease of the flux above the energy $10^{19.5}$ eV, which can indicate validity of the GZK effect. This stays in agreement with HiRes data on the contrary to AGASA observations (Fig. 2.8). The excess of AGASA events over this energy threshold is mostly explained by not appropriate energy calibration of the field of plastic scintillators. This surface detector was calibrated with strong dependence on simulations. On the other side, two fluorescence detectors at HiRes were using not well known atmosphere profile and fluorescence yield for their calibration. Nowadays, it seems that the latter experiment suffered by much lesser uncertainty than the former. These circumstances supported the motivation of hybrid PAO instrumentation with extended measurements of atmosphere profile as it will be described in the following chapter in more details. Another useful information about energy spectrum measured at PAO may be found in [19].

3.4.2 Anisotropy of the Most Energetic Cosmic Rays

In September 2007 paper about anisotropic distribution of cosmic rays of energy above 56 EeV detected at the PAO was published [20]. After statistical analysis the isotropy was excluded with more than 99 % probability.

In that time, there were indications that the sources of these events may be active galactic nuclei (AGN). Their correlation (Fig. 3.14) with events of energy above 56 EeV was accomplished by the assumption that the primary particles are protons. Due to large Larmor radius of proton little deviations of their arrival directions from directions of their sources were expected. Moreover only sources with strong acceleration potential (Fig. 2.3) located in near universe (GZK effect) could be taken under consideration and AGN were a good candidates. The analysis lied in minimalisation of the probability function depending on three variables. The maximal distance of AGN was set to 75 Mpc, energy threshold of showers to 56 EeV and the third variable, the angular distance, was calculated to be 3.1° during minimalisation of the probability function. This test method was applied for data obtained between 1.1. 2004 and 26.5. 2006. From next 13 detected events 8 were correlated with position of AGN while by the isotropic assumption only 2.7 were expected in average. This lead to mentioned exclusion of the isotropic flux of primaries at confidence level of 99 %.

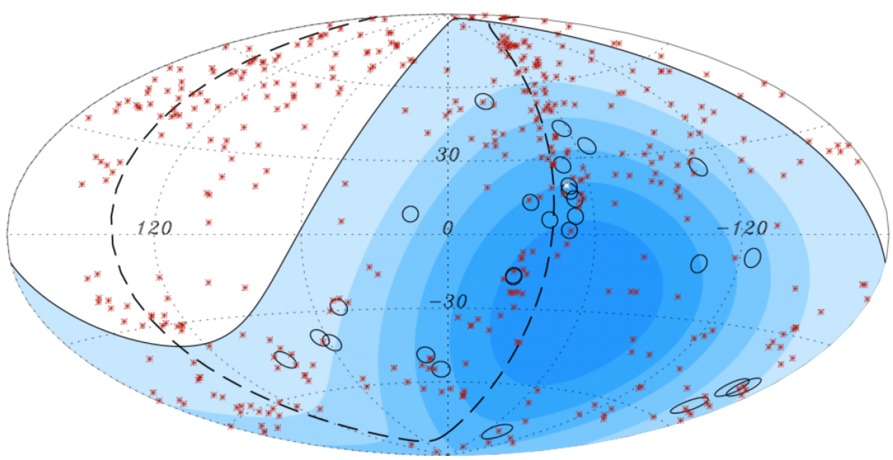

Figure 3.14: Celestial sphere in galactic coordinates together with positions of 27 events of energy greater than 56 EeV is shown. Events are located in the middle of rings with radius 3.1°. Positions of AGN closer than 75 Mpc are denoted by red crosses. The richness of blue color corresponds to relative PAO aperture and the line makes a boarder for PAO aperture for events with zenith angle upto 60°. Supergalactic plane is represented by the dashed line. The position of AGN in galaxy Centaurus A is marked by white cross. Picture is taken from [20].

Nowadays, it seems that many of these primaries can originate in only one source instead of many AGNs. The candidate is one of the closest AGN in galaxy Centaurus A ($\sim$ 4 Mpc). This hypothesis is in agreement also with heavier mass of primaries. Their trajectories would be more curved in extragalactic and galactic fields and therefore greater deviations from source direction are expected as may be seen in Fig. 3.15. Even if the origin of EHECR can be different than just from the nearby

AGNs, the proof of anisotropy as presented in [20] remains valid. Further data taking will be crucial for indication of possible sources. More information about anisotropy searches can be found in [21].

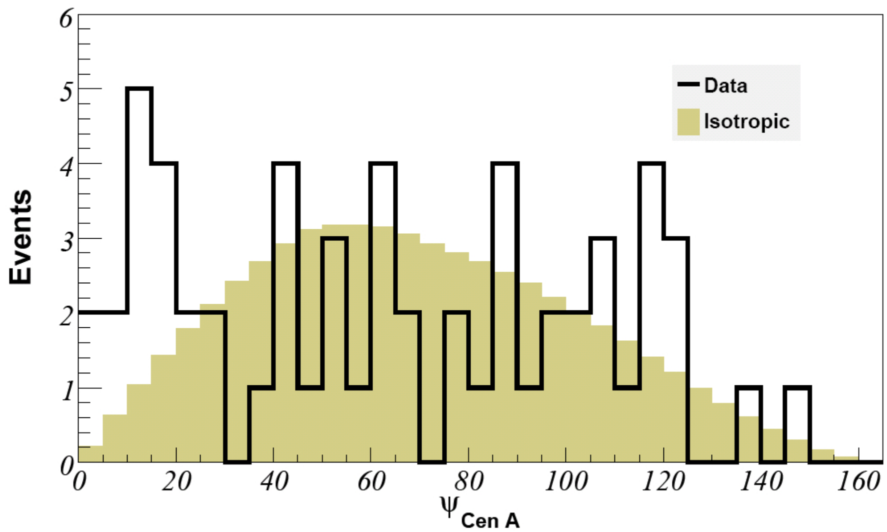

Figure 3.15: The histogram of selected events above 55 EeV as a function of angular distance to Cen A. The averaged isotropic expectation is shaded brown. Picture comes from [21].

3.4.3 Mass Composition of UHECR

As it was indicated in the previous text, indirect derivation of mass composition from air shower data is relied on simulations which are results of extrapolations from accelerator physics. The most used hadronic interaction models in simulations are QGSJET, SIBYLLL and EPOS. Their predictions assume that interactions do not change within the observed energy range too much. Showers induced by primaries of different mass (proton and iron for simplification) are mostly distinguished according to the position of X_{max} or according to the fraction of muons in secondary particles. The latter method is problematic to apply and therefore a project AMIGA is nowadays built to provide useful information about muon shower component. More information about AMIGA may be found in [22].

Study of binned averaged values of X_{max} distribution (Top Fig. 3.16) indicates that, according to simulations, up to energy 10^{19} eV cosmic rays are composed primarily of lighter nuclei but for higher energies PAO detects more heavier primaries. Errors of individual binned values are of statistical nature. More visible indication, that the average mass of cosmic rays increases, is shown in Bottom Fig. 3.16. Here the shower-to-shower fluctuations, RMS(X_{max}), are obtained by subtracting the detector resolution in quadrature from the width of the observed X_{max} distributions. It is also remarkable that there are considerable differencies between individual hadronic models. Thus not only larger statistical set of data is needed but also better understanding of interaction properties in ultra-high energy region will be crucial for the right interpretation of observed X_{max} distribution. More information about UHECR mass composition as it is measured at PAO is provided in [23].

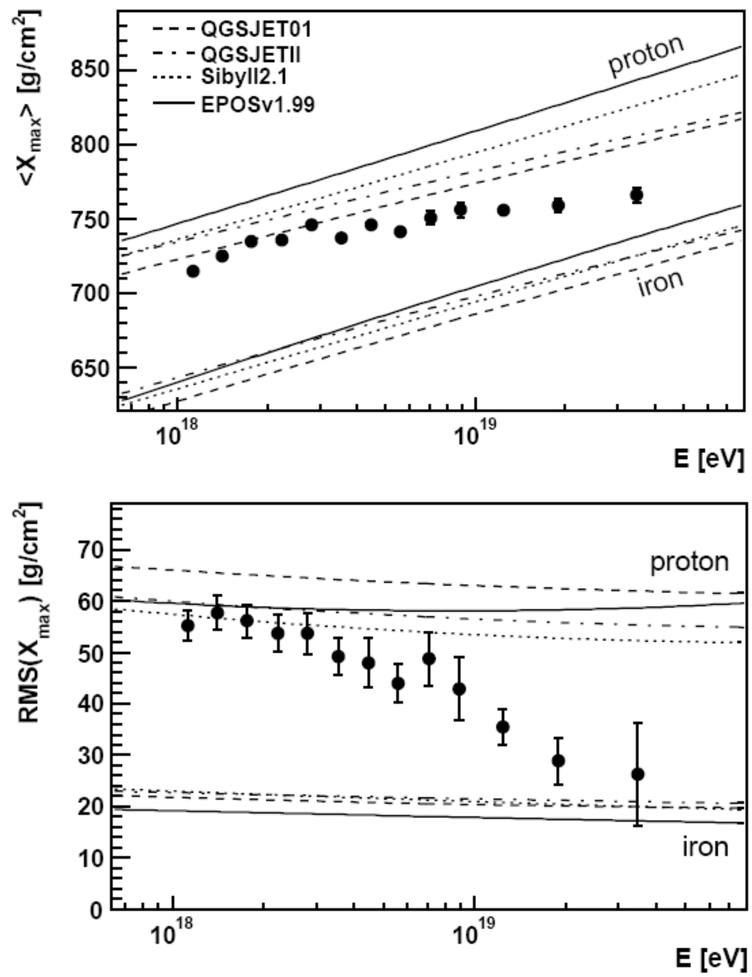

Figure 3.16: Distribution of mean values of X_{max} (**Top**) and $RMS(X_{max})$ (**Bottom**) measured at PAO. Simulated dependencies of proton and iron are shown for different hadronic interaction models. For reference see [24].

3.4.4 Limits on Photon Fraction of UHECR

To determine showers initiated by photons it is also needed to use comparison with simulations. The quantity X_{max} is used for this purpose again. Photons are predicted to penetrate deeper than nuclei and therefore for events with high X_{max} is searched (Top Fig. 3.17). There are 8 events which are denoted as photon candidates in the figure. Resulting upper limits on photon fraction of UHECR are presented in Bottom Fig. 3.17. Limits obtained by PAO are depicted together with other experiments using array of surface detectors. PAO is the first experiment setting limits on photon fractions of UHECR using fluorescence detection. It enabled to extend limits below 10 EeV, which was not possible so far. The PAO results in [25] decreased systematic uncertainties in the energy spectrum, nuclear primary composition and proton-air cross-section where photon fraction causes indispensable biases.

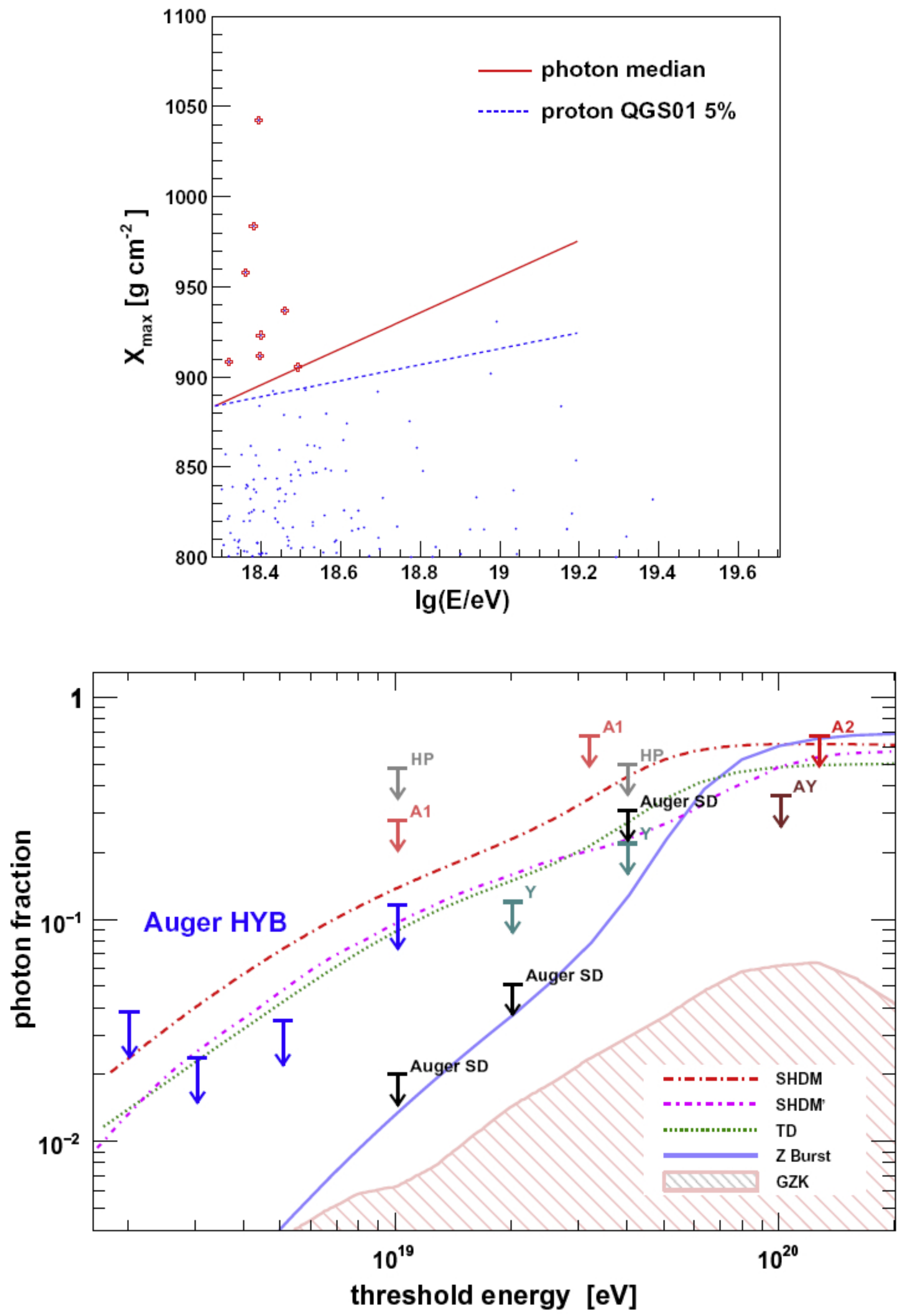

Figure 3.17: **Top:** Dependence of X_{max} above 800 g$\cdot$cm^{-2} on energy E of high quality hybrid events detected at PAO. Blue dashed line corresponds to the limit above which only 5 % of simulated (QGSJET01) events initiated by protons remained. Red line denotes median of distribution of simulated events initiated by photon. Red markers denote 8 candidate events for photon primaries. **Bottom:** Upper limits on the photon fraction in the integral cosmic ray flux of UHECR. Results from different experiments (AGASA-A, Yakutsk - Y, Haverah Park - HP) are also used. Limits are symbolised by arrows. PAO provides two independent settings of limits using SD events and hybrid events. The shaded region corresponds to the expected GZK photon fraction. Lines indicate various predictions from top-down models. Pictures is taken from [25]

Chapter 4

Energy Calibration at the Pierre Auger Observatory

To remove dependencies of results obtained at PAO on the models of hadronic interactions and atmospheric conditions a great attention is devoted to energy calibration. Energy calibration of the FD and SD is described in this chapter. Calibration of the SD signal to energy is studied as a primary aim of this thesis.

4.1 Energy Calibration of the FD

To determine shower longitudinal profile and energy it is needed to obtain a relation between ADC counts from individual photomultipliers of fluorescence telescope and light flux. There are three types of FD calibration at PAO: absolute calibration, relative calibration and calibration using laser shots in the atmosphere. For conversion of light flux to shower energy a detailed study of atmosphere and produced light by particle energy deposit in the atmosphere is performed at PAO.

4.1.1 Absolute Calibration

Several times per year the absolute calibration of all fluorescence telescopes is performed. A drum-shaped portable source of homogeneous light flux is attached (Fig. 4.1) to the bay entrance providing well measured light flux for all pixels of the fluorescence telescope. The uncertainty in drum intensity (6 %) together with temperature dependencies, camera response variation in time and spectral characteristics of the LED light source combine in the overall FD absolute calibration uncertainty of ~ 9 % [14].

Another type of absolute FD calibration is based on vertical laser shots which provide precisely calculable amount of photons scattered into the aperture of fluorescence telescope. A nitrogen portable laser (337 nm) providing 100 mJ pulses is used at distance 4 km from FD.

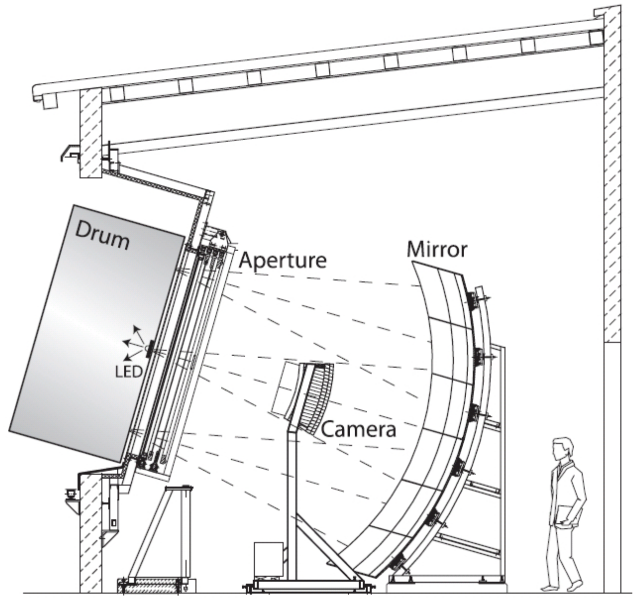

Figure 4.1: Schematic view of the absolute calibration of the fluorescence telescope using drum providing constant homogeneous light flux of known intensity. Picture comes from [14].

4.1.2 Relative Calibration

Before and after each night of operation a series of relative calibration measurements is performed. It is used to monitor detector response between drum calibrations. In three sources, depicted in Fig. 4.2, diffused light is produced.

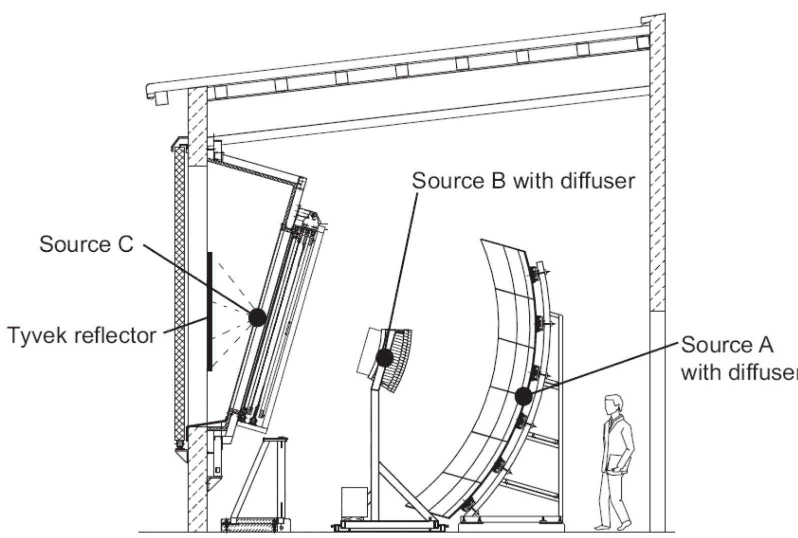

Figure 4.2: Schematic view of the relative fluorescence detector calibration. Positions of three light sources are shown. LED is used for A source and xenon flash lamps provides diffused light for sources B and C. Picture is obtained from [14].

4.1.3 Measuring of Atmosphere Profile

Some photons of fluorescence light originating near the shower path are scattered or absorbed in the atmosphere during their propagation to FD. Rayleigh scattering on air molecules dominates photon looses during their propagation. Another scattering process contributing to photon losses is the scattering on aerosol particles (Mie scattering), which is substantial especially in the lower part of atmosphere. At PAO several independent measurements of extinction using laser shots are performed to determine an amount of lost fraction of fluorescence photons. The term extinction means the loss of light in the atmosphere from a directly transmitted beam. Small absorbtion proceeds on ozone molecules in the upper part of the atmosphere but great absorbtion on carbon atoms arise when the atmosphere is full of smoke [1]. Following instruments are used to monitore atmospheric conditions above the field of surface detectors.

LIDAR: Near each of four FD sites a LIDAR (LIght Detection And Ranging) instrument is installed. It measures the backscattered light from UV laser pulses. Steering frame of LIDAR allows to point laser in arbitrary direction in the sky to provide aerosol measurement near the shower soon after succesful hybrid trigger. Together with LIDAR infrared camera detecting cloud-covering is installed at each FD site.

CLF: Central laser facility (CLF) is located in the middle of the array and provides UV laser test beam shots in the atmosphere every hour of FD measurement to study properties of the atmosphere and of individual FDs. Reconstructed light from laser shots permits measurement of important quantity, Vertical Aerosol Depth Profile (VAOD), which is a function of altitude. Each shot is tagged to avoid misinterpretation of neutrino-induced shower. CLF is also connected with tank via optical fiber to be able to analyse hybrid timing procedure and reconstruction precision.

HAM: HAM (Horizontal Atmospheric Monitoring) provides measuring of horizontal aerosol optical depth between individual FDs. It consists of UV light source and of CCD camera receiving signal from another HAM.

APF: APF (Aerosol Phase Function) is installed in front of each FD site. It measures the aerosol differential scattering cross-section by firing a horizontal, collimated beam of light from xenon flashlamp across the front of the FD site.

FRAM: Fotometric Robotic Atmospheric Monitor (FRAM) provides measurement of extinction knowing calibrated luminosity of star "candles". Thus, it measures the influence of whole atmosphere on UV light attenuation. Fram is also used for astronomical measurement.

[1] Unfortunately, in Argentinean pampa it is quite common during brushfire season.

The overall uncertainty of FD energy measurement is estimated in [19] to 22 %. The largest contribution to overall uncertainty arises from fluorescence yield (14 %). Effects of temperature, pressure and humidity of air add 7 %, detector calibration 9 %, atmospheric attenuation 4 %, shower reconstruction 10 % and invisible energy 4 %.

4.2 Energy Calibration of SD

The uniqueness of the SD energy calibration lies in its direct independence on the hadronic interaction models on which it relied in all previous surface detector experiments studying high energy cosmic rays. This is achieved due to the precise FD energy measurement of high quality golden events (hybrid events which can be reconstructed also by SD only). However, since FD measures only the deposited calorimetric energy it is needed to convert it to the shower energy using correction for fraction of shower energy carried away by muons and neutrinos (mostly denoted as invisible or missing energy). The correction factor is obtained as average missing energy from simulated showers initiated by proton and iron at equal rate. This factor depends on energy [2], on used hadronic model and on shower-to-shower fluctuations. For energy 10^{19} eV the fraction of invisible energy was averaged to $\sim$ 10 % (Fig. 4.3). Estimated systematic uncertainty due to invisible energy brings 4 % to the complete systematic uncertainty of FD energy calibration. This is the only assumption made from simulations that is used for SD and FD energy calibration at PAO.

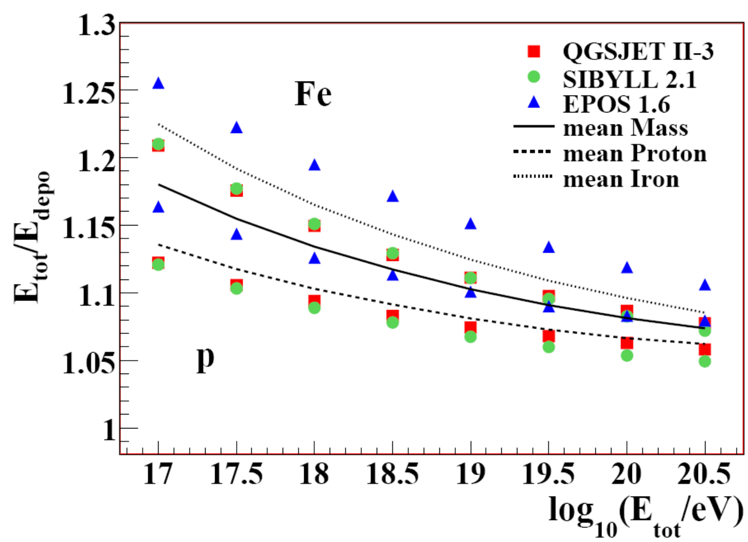

Figure 4.3: Factor used for conversion of calorimetric energy to total shower energy is shown for various hadronic models. Mean conversion factor for iron (dotted line), proton (dashed line) and for mean mass (full line) are calculated. Picture is taken from [26].

[2]Lifetime of mesons is energy dependent and so does the number of muons that need long path to interact and the number of neutrinos which escape undetected.

As it was mentioned above, for conversion of SD signal ($S1000$) to energy, at first, it is needed to convert $S1000$ to signal which would be produced by the same shower of zenith angle 38° ($S38$). A shower of small zenith angle produces larger signal $S1000$ than a shower of large zenith angle, since the shower of small zenith angle has shorter path in the atmosphere and therefore the electromagnetic component of such shower has stronger contribution to the SD signal. The curve describing the attenuation of $S1000$ with zenith angle is produced applying the so called Constant Intensity Cut (CIC) method. Thus, measuring of $S1000$ and zenith angle of shower, the SD energy estimator $S38$ is obtained using attenuation curve.

4.2.1 Attenuation Curve

The attenuation curve describes the dependence of $S1000(\Theta)$ on the zenith angle Θ (or on a function of the zenith angle [3]) for a given primary particle energy. This dependence can be acquired from the simulated data (AGASA) or from the real data using the CIC method (PAO). The attenuation curve, $CIC(\Theta)$, is defined via equation:

$$S38 = \frac{S1000(\Theta)}{CIC(\Theta)}\,. \tag{4.1}$$

In this thesis the $CIC(\Theta)$ is a quadratic function of $cos^2(\Theta)$:

$$CIC(\Theta) = 1 + a \cdot x + b \cdot x^2 \tag{4.2}$$

where x = $cos^2(\Theta) - cos^2(38°)$ and a, b are real constants [4].

Constant Intensity Cut Method

The Constant Intensity Cut method assumes the isotropic flux of primary cosmic ray particles above a given energy. Separating low energy events the remaining data set rests isotropic, which is the crucial idea of the method. The originally used technique plots the event flux for bins of $cos^2(\Theta)$ for various event selections. This selection is determined by different minimum value of the parameter $S1000$ (Fig. 4.4). The intersections of the curves (corresponding to different minimal values of $S1000$) with a horizontal line, given by the chosen flux, forms the attenuation curve. The resulting attenuation curve is dependent on the chosen cut, size of a bin and also on the precision with which the intersections are actually found.

Another technique lies in sorting $S1000$ values from the largest to the lowest value for every bin of $cos^2(\Theta)$. Choosing the N^{th} value (cut) of the $S1000$ for every ordered zenith angle bin, the attenuation curve is set. The applied cut corresponds to the particle flux similarly as it is in the original method and is therefore denoted as "flux cut". This method was used for producing attenuation curves in the

[3] Mostly $cos^2(\Theta)$ is used since a bin of $cos^2(\Theta)$ corresponds to the element of space angle for horizontal array.

[4] Alternative form $CIC(\Theta) = A \cdot x^2 + B \cdot x + C$ where A, B, C are fit parameters and $x = cos^2(\Theta)$, is also used in this thesis for fitting of attenuation curves. However, since $CIC(38°)$ is fixed to be unity, parameters A, B and C are correlated. It was checked that these fits give same results as usage of eq. (4.2) where parameters a, b are independent.

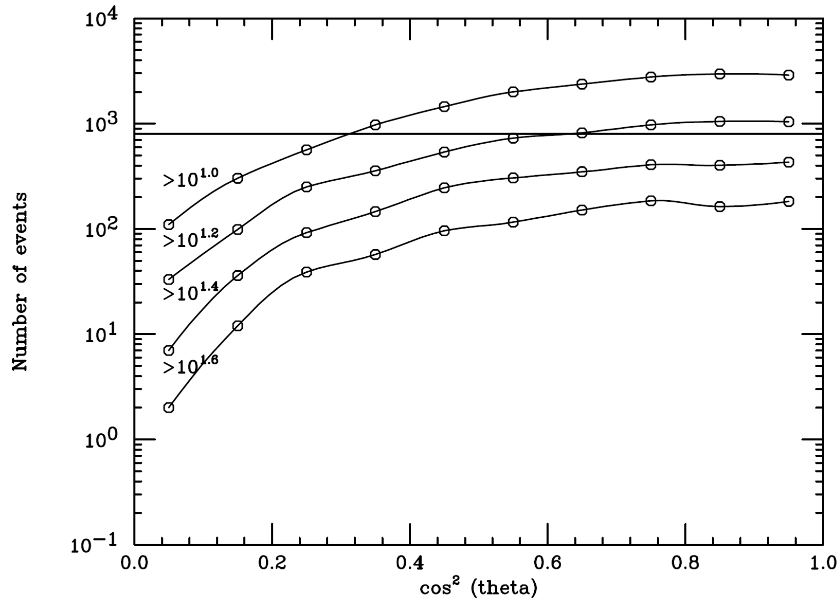

Figure 4.4: Plot of integral number of events vs. $cos^2(\Theta)$ for the indicated minimum value of $S1000$. The horizontal line represents constant flux. Intersections of this line with graphs from the attenuation curve. Picture comes from [27].

presented thesis and represents the first part of author's original results. The attenuation curve is then dependent on a chosen value of flux cut and on a size of zenith angle bin [5].

Chosen SD Data Set

For creating attenuation curves following cuts were applied on SD events to satisfy isotropic feature of incoming cosmic ray directions and also to allow for as large set of data as possible to minimalise point errors. These errors originate in Poisson distribution of sorted events in individual zenith angle bins and therefore differences between the N^{th} and $(N \pm \sqrt{N})^{th}$ values of $S1000$ were used for calculating error bars for every bin.

- Only events with reconstructed zenith angle and LDF were considered. They had to fulfil additional condition for relative error of $S1000$ within 50 %, which removed remaining wrong reconstructed events.
- Zenith angle $\leq 60°$, which together with energy threshold $3 \cdot 10^{18}$ eV ensures almost 100 % shower detection efficiency. The aim is thus to calibrate SD for energy greater than $3 \cdot 10^{18}$ eV.
- Events recorded during so called "bad periods" were excluded. Bad period denotes time interval during which SD was not reliably operational.

[5]But only to some extend as will be seen in the next chapter.

- Accomplishing of T4 and T5 trigger conditions was applied to ensure good reconstruction ability of detected shower.

Cut	**Remaining events**
None	2 127 092
Bad periods	2 063 662
Zenith $\leq 60°$	1 968 735
T4 + T5	1 501 033
$S1000$ rel. error ≤ 50 %	1 500 114

Table 4.1: Quality cuts applied on SD data set together with number of surviving events.

Employing quality cuts (Tab. 4.1), the attenuation curve (Fig. 4.5) normalized to zenith angle 38° ($cos^2(\Theta) \cong 0.62096$) was obtained from SD data [6] collected at PAO from 1.1. 2004 to 31.1. 2010. Normalized curves are suitable for the curve shape determination due to the elimination of the signal size energy dependence. Cut of value 600 was chosen and corresponds approximately to the flux of cosmic rays of energy greater than 7 EeV. The $CIC(\Theta)$ drawn in Fig. 4.5 has following form:

$$CIC(\Theta) = 1 + (0.87 \pm 0.02) \cdot x + (-1.37 \pm 0.11) \cdot x^2 \tag{4.3}$$

where $x = cos^2(\Theta) - cos^2(38°)$.

4.2.2 Calibration Curve

As it has been already mentioned, the signal $S38$ is proportional to the energy. The proof of this statement is presented in Fig. 4.6. Since the FD provides very precise measurement of shower energy (E_{FD}), it is used to calibrate $S38$ parameter. The calibration curve describing relation between $S38$ and E_{FD} has following general form:

$$S38 = a \cdot E_{FD}^b \tag{4.4}$$

where a and b are constants determined from the fit. Taking logarithm to (4.4) the fitted function acquires simple linear form, which was used for drawing of calibration curve in Fig. 4.7.

Chosen Golden Data Set

The sample of hybrid events is much smaller compared to the sample of SD only events. Moreover it is necessary to use another selection criteria on data coming from FD to ensure the best possible reconstruction precision. On the other hand, the cuts need not to be too tight to keep sample of events large enough to allow some reliable conclusions. Following cuts on golden data were used:

[6] ADST data format was used for analysis.

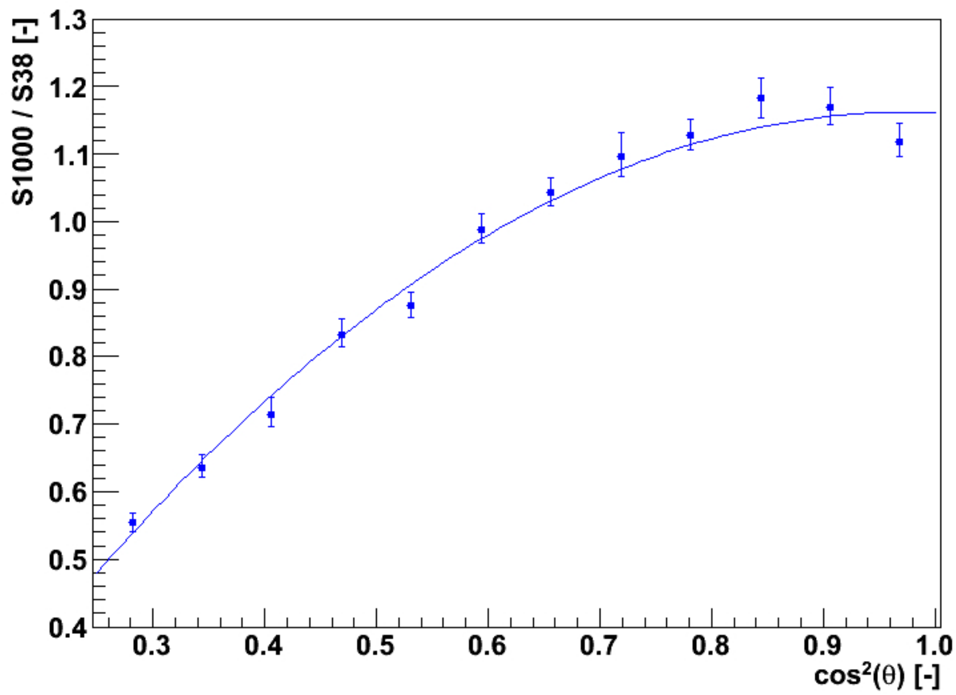

Figure 4.5: The normalized attenuation curve as a function of $cos^2(\Theta)$ used for SD energy calibration. A flux cut of value 600 was chosen to correspond energy $\sim$ 7 EeV.

- Same SD quality cuts as for the attenuation curve were used except for zenith angle condition. For conversion of $S1000$ to $S38$ zenith angle reconstructed by FD was applied.
- The FD zenith angle $\leq 60°$ was employed.
- SD station of highest signal used for hybrid reconstruction has to lie within 750 m from shower axis. This cut suppresses hybrid events with random SD trigger.
- Vertical aerosol optical depth (VAOD) measured by CLF at reference height less than 0.1.
- X_{max} has to lie in Field of View (FOV) of the fluorescence telescope.
- Cherenkov fraction of the detected light does not exceed 50 %.
- The reduced χ^2 of G-H fit of the longitudinal shower profile less than 2.5. It should remove wrong reconstructed shower profile due to presence of fog or cloud.
- The reduced χ^2 of G-H exceeds the simple linear fit by at least four. It supports good quality of profile reconstruction.
- LIDAR data of aerosol measurement and cloud detection are available.

- The presence of clouds may seriously disturb shower reconstruction and thus cloud coverage less than 25 % is demanded.
- Uncertainty of the FD energy (E_{FD}) less than 20 %.
- Uncertainty of the X_{max} better than 40 g$\cdot$ cm^{-2}.
- Hole in the atmosphere depth profile ≤ 20 % was chosen to reject events detected by more than one telescope where substantial fraction of shower light is lost at telescope view boundaries.

Cut	**Remaining events**
None	85 951
Bad periods	84 160
T4+T5+SD rec. level	59 091
$S1000$ rel. error	59 011
FD rec. level	54 392
$E_{FD} \geq 10^{18}$ eV	22 587
Zenith angle ≤ 60°	19 785
E_{FD} rel. error ≤ 20 %	15 126
X_{max} error ≤ 40 g$\cdot$cm^{-2}	11 710
X_{max} in FOV	11 226
Hottest SD station to axis ≤ 750 m	10 237
G.-H. red. ≤ 2.5	9 898
G.-H. + 4 ≤ lin. fit	8 250
Cher. fraction ≤ 50 %	8 132
VAOD available	8 132
VAOD at ref. height ≤ 0.1	7 971
LIDAR data available	3 714
Cloud coverage ≤ 25 %	2 357
Hole in depth profile ≤ 20 %	2 337

Table 4.2: High quality cuts applied on golden data set together with number of remaining events. These events were collected at PAO from 1.1. 2004 to 31.1. 2010.

From events satisfying quality cuts (Tab. 4.2) there are at first chosen events of FD energy greater than 3 EeV for drawing of calibration curve. However, not to exclude events with a bit smaller reconstructed FD energy but producing a comparable signal in SD as usual events of energy ≥ 3 EeV, it is necessary to use perpendicular cut. Iteratively it is found a line perpendicular to the calibration curve. It has to intersect the calibration curve in a value corresponding to energy 3 EeV (Fig. 4.6). Events situated above this line are used for drawing of final calibration curve (Fig. 4.7). For conversion of $S1000$ to $S38$ the attenuation curve, eq. (4.3), was used. Reconstructed quantities of showers detected independently by more fluorescence telescopes were averaged to satisfy calibration using individual hybrid showers and to avoid possible redundancies in the data set due to stereo, triple or

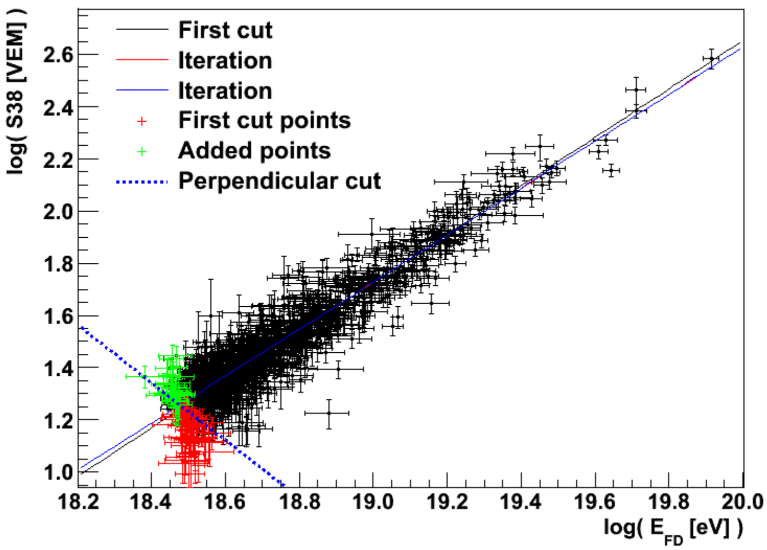

Figure 4.6: Individual iteration steps in derivation of calibration curve. Last two iterations are not able to be distinguished by eye. Perpendicular cut of last iteration is also shown together with rejected and added points with respect to the first cut at 3 EeV.

quadrupole FD detection [7]. The uncertainty of $S38$ for each event was assumed to be composed of $S1000$ uncertainty, σ_{S1000} (finite size of the detector, LDF shape assumption, shower-to-shower fluctuations), uncertainty of $CIC(\Theta)$ curve shape ($\sigma^{SHAPE}_{CIC(\Theta)}$) and uncertainty given by error of measured zenith angle ($\sigma^{ZENITH}_{CIC(\Theta)}$). The resulting relative uncertainty of $S38$ was thus expected to be formed by three independent contributions:

$$\left(\frac{\sigma_{S38}}{S38}\right)^2 = \left(\frac{\sigma_{S1000}}{S1000}\right)^2 + \left(\frac{\sigma^{SHAPE}_{CIC(\Theta)}}{CIC(\Theta)}\right)^2 + \left(\frac{\sigma^{ZENITH}_{CIC(\Theta)}}{CIC(\Theta)}\right)^2 . \tag{4.5}$$

Uncertainty of $CIC(\Theta)$ curve shape will be described in details in next chapter. It is worth to mention that contributions of relative uncertainties from attenuation curve shape and measuring of zenith angle are much smaller than the dominant relative uncertainty of $S1000$.

Corresponding parameters of eq. (4.4) are: $a = (1.22 \pm 0.20) \cdot 10^{17}$ eV and $b = 1.109 \pm 0.007$. In Fig. 4.8 relative differences between calibrated SD energy and FD energy are shown in the histogram. The fitted gaussian is of width (17.0 ± 0.7) %. This number should reflect reconstruction uncertainty of FD energy combined with size of shower-to-shower fluctuations of $S38$.

This calibration curve (Fig. 4.7) was derived applying strict cuts (Tab. 4.2) and only quite small data set passed, which was a prise for good precision achieved. However, for studying various detailed aspects of SD calibration curve in the next chapter it is more appropriate to use data without demand

[7]The event detected by two FDs is denoted as stereo event, similarly triple (3 FDs) and quadruple (4 FDs) events. Showers detected by only one FD are known as so called mono events.

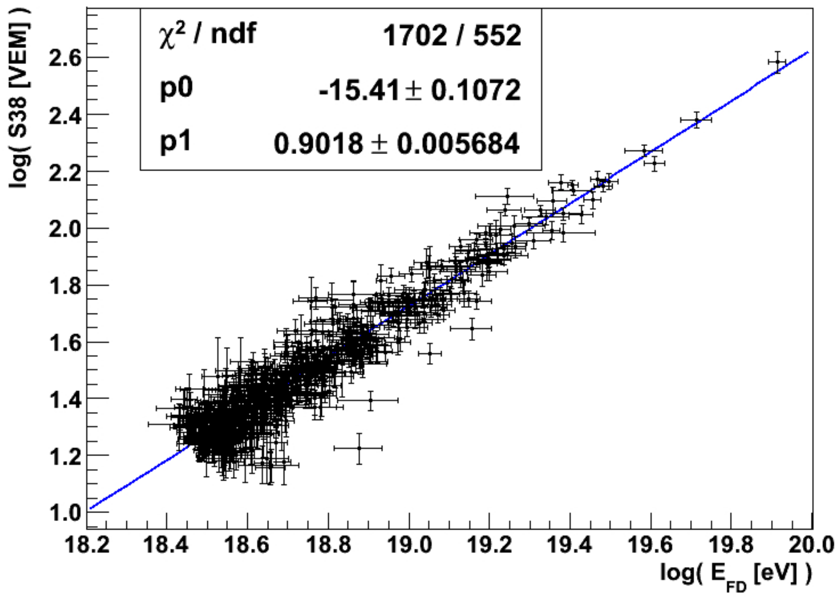

Figure 4.7: Plot of the SD energy calibration. The dependence of the logarithm $S38$ on the logarithm of the fluorescence energy $E_{FD} \geq 3 \cdot 10^{18}$ eV is shown for 554 high quality golden events detected at PAO. The perpendicular cut corresponding to energy 3 EeV was used.

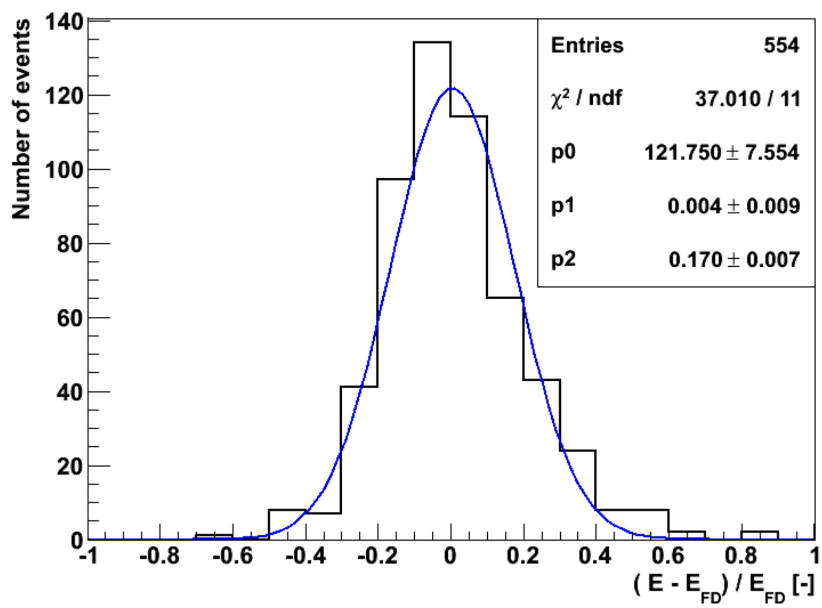

Figure 4.8: Histogram containing differences of E_{FD} from calibrated SD energy (E) relative to E_{FD}. Fitted gauss distribution with parameters is shown.

for cloud fraction ≤ 25 %. Releasing this cut larger data set of more than 50 % events was obtained. Constants of calibration curve (Fig. 4.9) from this broader data set are comparable to constants obtained from Fig. 4.7 as it is shown in Fig. 4.11 and Tab. 4.4. The width of fitted gaussian distribution in Right Fig. 4.9 is about 1.4 % worse but still maintain the center of gaussian near zero.

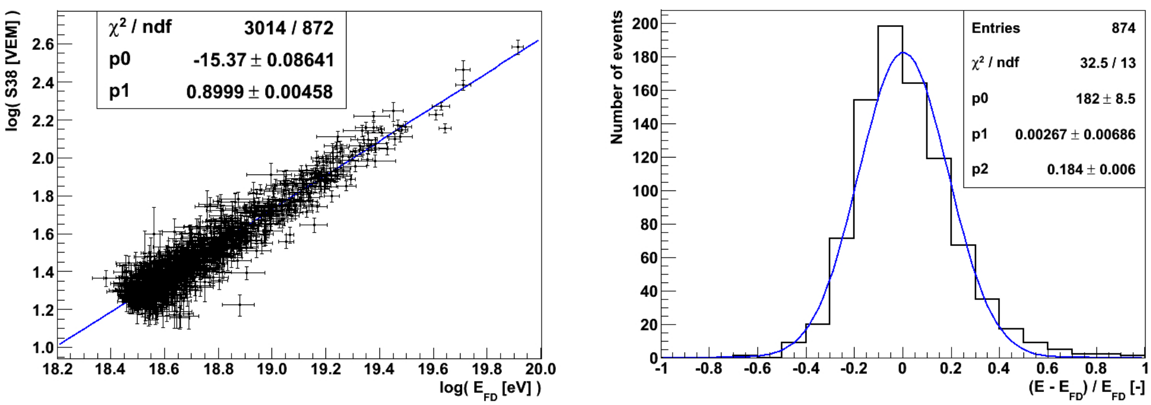

Figure 4.9: **Left:** SD calibration curve obtained without demand for cloud fraction ≤ 25 %. **Right:** Histogram showing distribution of relative differences of E_{FD} from calibrated SD energy (E) relative to E_{FD}. Fitted gauss distribution with parameters is shown.

4.2.3 Comparison of Achieved SD Calibration with Official PAO Results

As it was mentioned above, the SD energy calibration process obtained from PAO data proceeds in two steps. Therefore not only the resulting calibration curve but also the attenuation curve was confronted with official PAO results.

In Fig. 4.10 the comparison of attenuation curve obtained in [19] and attenuation curve of the same binning used in this thesis for calibrating process is depicted. They are quite good correlated which supports the validity of method used for drawing attenuation curves in this thesis. Curves are equal for zenith angle 38° from definition of used normalization. Slight differences are mainly caused by different sizes of used SD data set. In this thesis data collected during more than one year longer period were considered. For comparison, values of fitted parameters in eq. (4.2) are introduced in Tab. 4.3.

From Fig. 4.11 it can be seen that calibration curve obtained employing strict and less strict cut conditions correlate quite well with curve presented in [19]. Differences are mainly caused by a bit different set of selected events. Moreover, for derivation of mentioned attenuation curves systematic uncertainties such as dependence on atmospheric conditions were not considered in this thesis. The resulting calibration constants (Tab. 4.4) agree within fit uncertainties with constants obtained in [19]. Influence of atmosphere conditions on calibration curve will be studied separately in the next chapter.

Calibration curve obtained from strict cuts shows comparable precision with [19] considering gaussian distributions of relative differences between calibrated energy and FD energy.

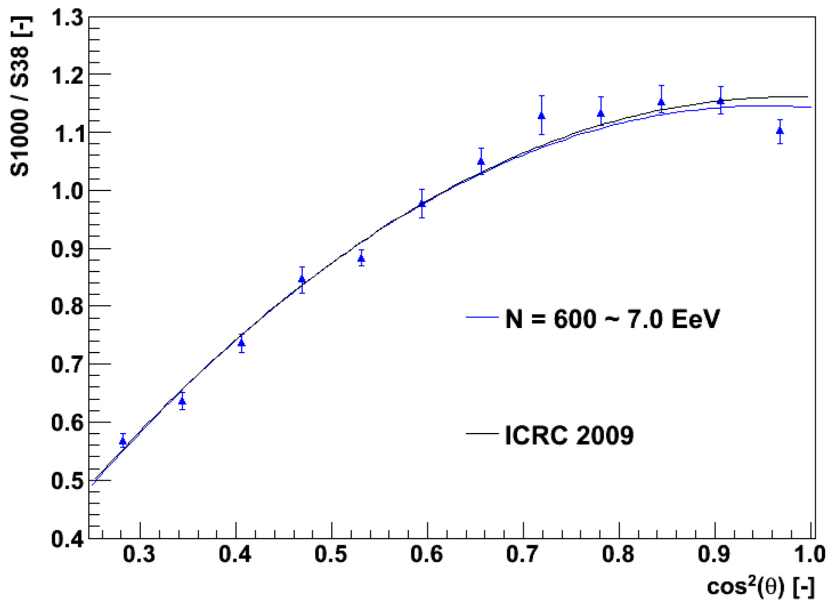

Figure 4.10: The normalized attenuation curve as a function of $cos^2(\Theta)$ compared with attenuation curve from [19].

Curve	a [-]	b [-]
ICRC 2009	0.90 ± 0.05	-1.26 ± 0.21
Thesis	0.87 ± 0.02	-1.37 ± 0.11

Table 4.3: Parameters of attenuation curve in eq. (4.2) used in the thesis and of attenuation curve obtained in [19].

The differences between calibrated SD energies for individual events obtained in this thesis compared to official SD energies reach 10 % at 3 EeV, 5 % at 10 EeV and are negligible at 50 EeV. It is worth to mention that the observed differences can originate also in the usage of perpendicular cut in this thesis contrary to more sophisticated so called "elliptical" cut in the official calibration procedure. Another effect can originate in the fitting procedure. However, the resulting distributions of $(E - E_{FD})/E_{FD}$ obtained in this thesis are similar to official one.

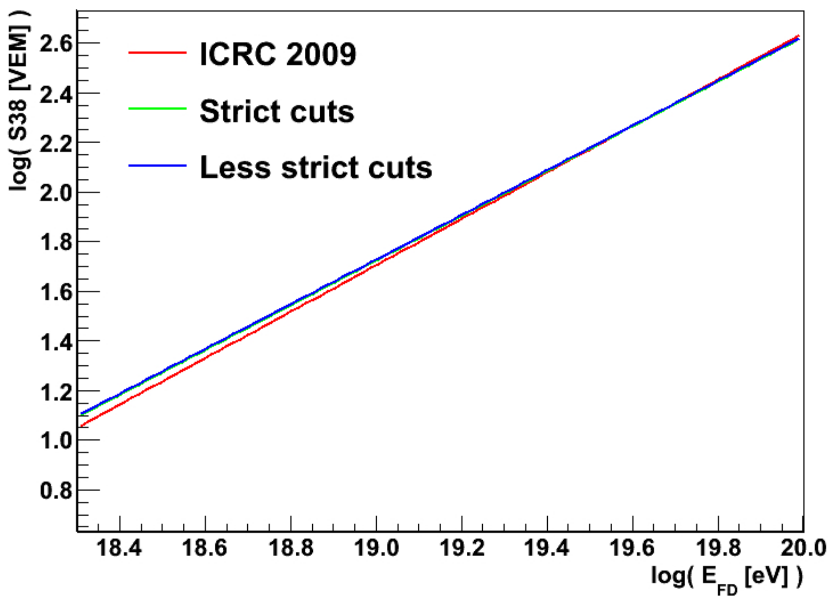

Figure 4.11: Calibration curves from Fig. 4.7 and Fig. 4.9 (not distinguishable by eye) compared with calibration curve obtained in ICRC 2009 [19].

Curve	**a [10^{17} eV]**	**b [-]**	**Mean [%]**	**Width [%]**
ICRC 2009	1.51 ± 0.13	1.070 ± 0.041	2.0 ± 1.0	17.0 ± 1.0
Strict cuts	1.22 ± 0.20	1.109 ± 0.007	0.4 ± 0.9	17.0 ± 0.7
Less strict cuts	1.20 ± 0.16	1.111 ± 0.006	0.3 ± 0.7	18.4 ± 0.6

Table 4.4: Parameters of calibration curves from Fig. 4.7 (Strict cuts), Fig. 4.9 (Less strict cuts) and from [19]. Parameters correspond to eq. (4.4). Last two columns contain two from three parameters describing fitted gaussian distribution of relative differences of calibrated energy from FD energy.

Chapter 5

Aspects of SD Energy Calibration

In this chapter various crosschecks of the attenuation curve and calibration curve stability represent the second part of author's original results. Various dependencies of the attenuation curve and calibration curve on used cuts and influence of atmosphere conditions are studied. The experimental attenuation curves are also compared to curves obtained from simulations. Moreover, sensitivity of calibration curve on position of shower maximum is investigated.

5.1 Variations of the Attenuation Curve

The main uncertainty of employed CIC method emerges from choice of the flux cut value and size of the bin $cos^2\Theta$. Attenuation curves for different cut values and bin size together with their variations during individual seasons of the year are studied in this section. Further, attenuation curves obtained from simulated showers of proton and iron primaries are compared with CIC curve drawn from PAO data.

5.1.1 Flux Cut Dependence

The most important feature of the attenuation curve [1] is its stability with arbitrary chosen value of the flux cut as it follows from Left Fig. 5.1. Deviations (Right Fig. 5.1) within 4 % ($\sigma_{rel.,cut}$) were observed for many various values of the cut.

Cuts for drawing of curves in Fig. 5.1 were chosen to satisfy isotropic flux of selected events (corresponding energy ≤ 50 EeV) and their 100 % detection efficiency (corresponding energy ≥ 3 EeV). The stability of CIC curve is crucial for conversion of $S1000$ to $S38$ since the same form of CIC curve is used for wide range of energy.

[1] Under attenuation curve is meant the normalized curve at 38°. Therefore for showers of different energy the same shape of attenuation curve is used for conversion to $S38$.

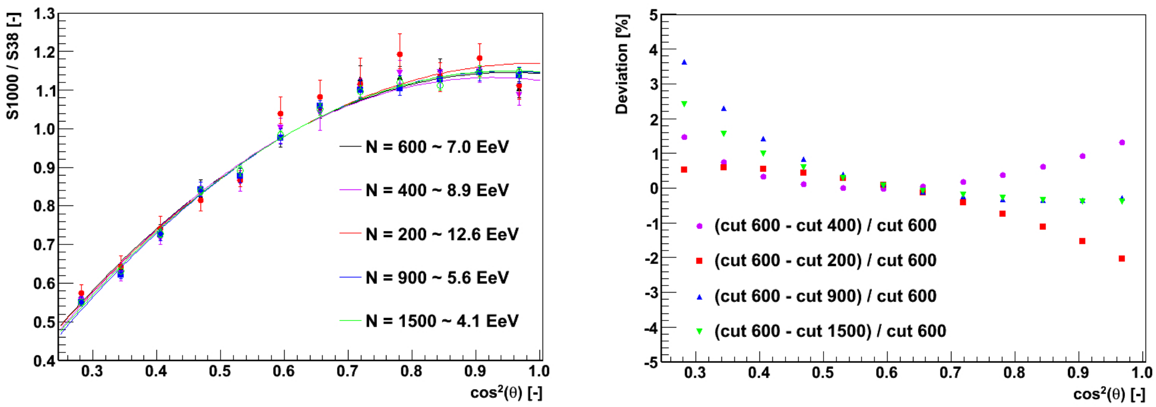

Figure 5.1: **Left:** Normalized attenuation curves drawn for different value of the cut N. **Right:** Relative differences of attenuation curves corresponding to cut N from attenuation curve obtained for cut N = 600.

5.1.2 Binning Dependence

The second contribution to the uncertainty of CIC curve shape arises from chosen size of bin $cos^2\Theta$. In Left Fig. 5.2 there are drawn 7 attenuation curves derived from different binning in $cos^2\Theta$. Only small variances within 3 % ($\sigma_{rel.,bin}$) were observed between curves for vertical (Θ near 0°) and horizontal (Θ near 60°) ends of the curve, which is explicitly illustrated in Right Fig. 5.2. The dependence of $CIC(\Theta)$ curve on chosen size of bin $cos^2\Theta$ is a bit weaker than on chosen flux cut. All together, the

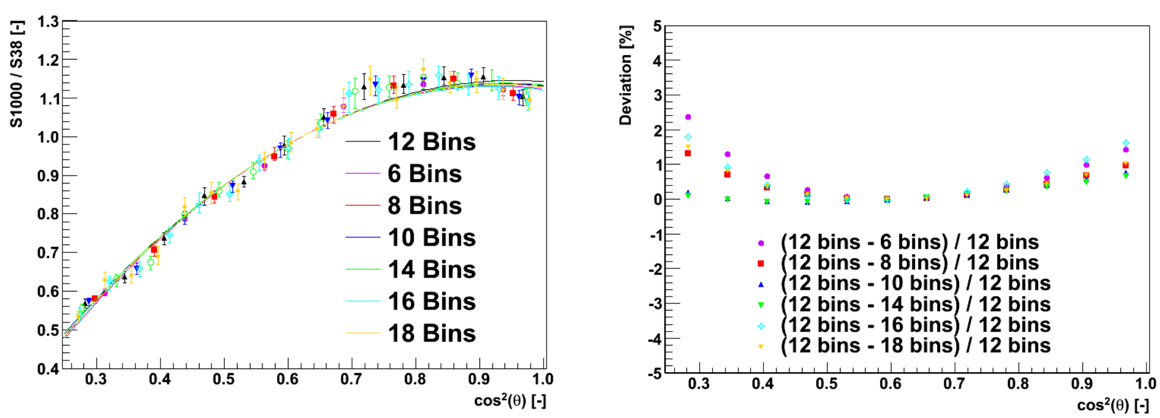

Figure 5.2: **Left:** Normalized attenuation curves drawn for different value of the bin $cos^2\Theta$. **Right:** The differences of attenuation curves corresponding to chosen number of bins of same width for whole range of zenith angle Θ up to 60°. CIC curves were obtained for flux cuts to correspond $\sim$ 7 EeV.

overall relative uncertainty of $CIC(\Theta)$ curve shape was estimated as

$$\left(\frac{\sigma^{SHAPE}_{CIC(\Theta)}}{CIC(\Theta)}\right)^2 = (\sigma_{rel.,cut})^2 + (\sigma_{rel.,bin})^2 \tag{5.1}$$

to be ~ 5 % at both horizontal and vertical ends of the curve.

To propagate uncertainty of $CIC(\Theta)$ curve to $S38$ parameter (eq. (4.5)), the dependence (Fig. 5.3) of $\sigma_{rel.,CIC(\Theta)^{SHAPE}}$ on $cos^2\Theta$ was assumed to be linearly decreasing from 5 % at $\Theta = 60°$ to zero at $\Theta = 38°$ and similarly linear increasing from the latter value to 5 % again for vertical events.

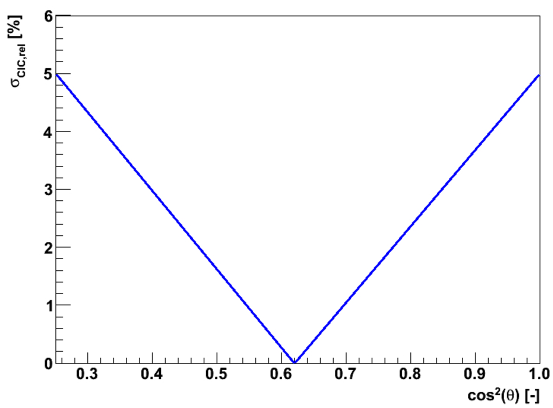

Figure 5.3: The dependence of used relative uncertainty of $CIC(\Theta)$ on $cos^2\Theta$.

5.1.3 Attenuation Curve from Simulated Data

The data obtained from simulations for showers initiated by proton and iron (Fig. 5.4) were also used for derivation of attenuation curve. Higher fluctuations in SD signal for proton than for iron may be noticed. The primary particles were set to have the energy 10 EeV and the zenith angle of produced showers was chosen in steps in $cos^2(\Theta)$ from 0.25 to 1. This data were simulated by the Czech Group of AUGER experiment in CORSIKA program. The hadronic interaction model EPOS 1.66 was used for high energy collisions and the model FLUKA was used for the low energy hadronic processes in the shower development. In the end, the outputs from CORSIKA were used in the program Offline for simulating the resulting signal in the surface detector.

In Fig. 5.4 it can be seen that for showers of same energy event-by-event fluctuations grows with decreasing zenith angle. The vertical showers contain larger contribution of electromagnetic component, which is of very fluctuating nature, on the contrary to SD signals of more inclined showers. With decreasing zenith angle the fraction of muons grows up, which maintain the SD signal more stable.

Shapes of the attenuation curves (Fig. 5.5) for proton and iron are in agreement with real data only in a region about 38° which is however assured from the definition of normalization. For inclined events both curves from simulated data fall faster then the curve from real data, which may be an

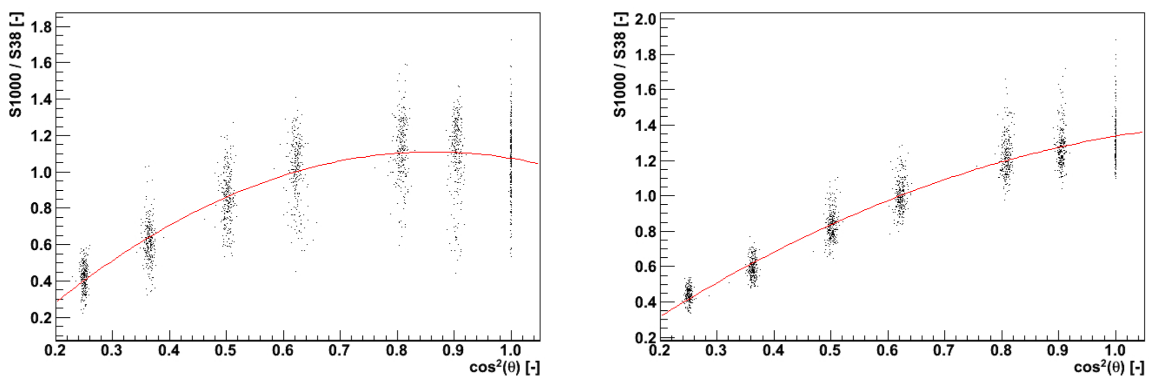

Figure 5.4: Simulated values of the $S1000$ (normalized to 38°) in dependence on $cos^2(\Theta)$ for showers initiated by proton (**Left**) and iron (**Right**) of energy 10 EeV. The fitted attenuation curves from 1 716 (proton) and 1 684 (iron) simulated events are shown.

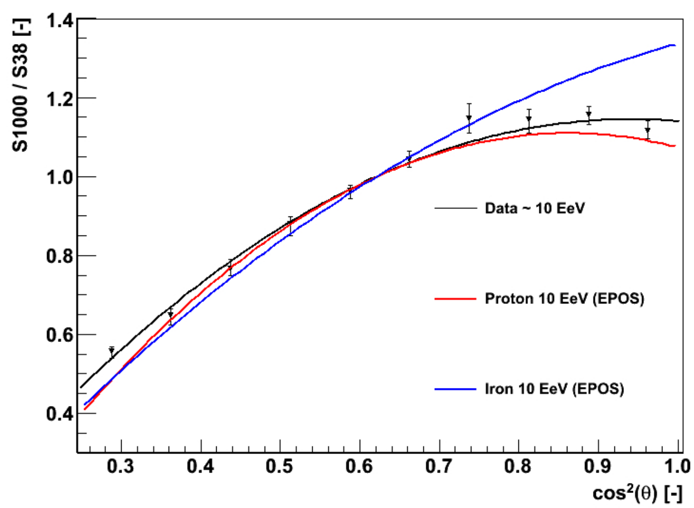

Figure 5.5: Comparison of the attenuation curves from simulated showers initiated by proton and iron of energies 10 EeV with the attenuation curve set from experimental data using the cut corresponding to energy ∼ 10 EeV. Curves are again normalized to satisfy the condition $S1000(38°) = 1$.

indication of lack of muons in hadronic interaction model EPOS 1.66 with respect to the observed showers. This is a bit surprising, since EPOS 1.66 produces more muons in comparison with another models of hadronic interactions. For vertical showers the "flattening" is remarkable for experimental data. It seems that this trend is rather followed by simulated data for protons whereas the attenuation curve for iron nuclei increases steeply over the attenuation curve for experimental data. Regardless, neither of both curves from simulated data describes the shape of attenuation curve from experimental data adequately.

5.1.4 Atmosphere and Time Variances

According to the Fig. 5.6 there have been chosen 4 seasons, for which the atmosphere pressure and density have similar behaviour. The atmosphere density shows lesser fluctuations and therefore its periodic behaviour is more obvious on the contrary to behaviour of atmosphere pressure. Data obtained during 12., 1. and 2. month of the year were denoted [2] as summer data and analogously other seasons were distinguished: autumn (3., 4., 5.), winter (6., 7., 8.) and spring (9., 10., 11.).

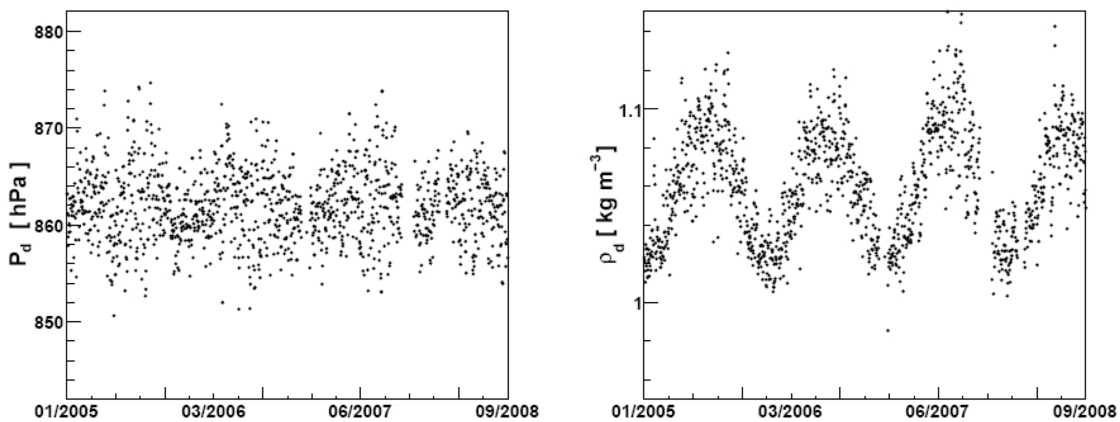

Figure 5.6: Variances of atmospheric pressure (p_d) and density (ρ_d) above PAO during almost three years. Seasonal trends are more obvious in right figure. Picture comes from [28].

In Left Fig. 5.7 it is shown that attenuation of signal $S1000$ during summer seasons shows different decrease with zenith angle wrt. other seasons for similar value of the flux cut. The possible explanation of observed effect is that the air density determines the lateral spread of electromagnetic component. Therefore, when the air density is lower during summer (Right Fig. 5.6), the LDF signal at 1 km from the axis contains greater contribution of electromagnetic component and is higher than during other seasons with higher average air density. The deviations of attenuation curve (Right Fig. 5.7) for different seasons wrt. attenuation curve derived from whole data sample reach even 10 % for summer period at $\Theta = 0°$ and $\Theta = 60°$.

5.2 Stability of the Calibration Curve

To study stability of calibration curve the choice of low energy cut, influence of shower maximum position, used FD station and variable atmospheric conditions during year were considered. As it was mentioned in the previous chapter, more events are required for such analysis and therefore events satisfying all cut conditions but releasing cloud coverage cut were employed (Fig. 4.9).

[2]On the southern hemisphere seasons are opposite to the seasons on the northern hemisphere.

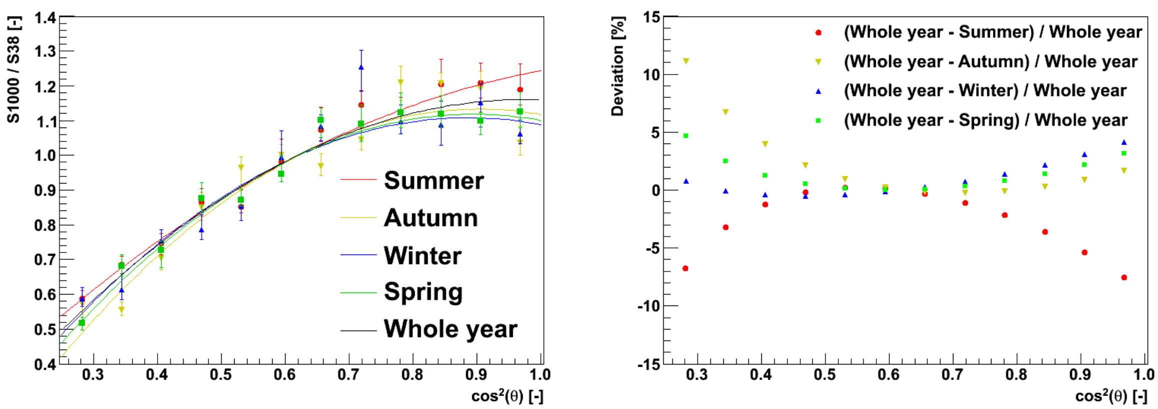

Figure 5.7: **Left:** Normalized attenuation curves obtained from data collected during different seasons of the year. For comparison, CIC curve performed from whole year is shown. All curves corresponds to similar flux cut value of 7 EeV. **Right:** Relative differences of attenuation curves obtained during different seasons from attenuation curve derived without season consideration.

5.2.1 Energy Cut Dependence

Previous calibration curves were produced applying perpendicular cut in a point of curve corresponding to 3 EeV. Changing this value to 5, 7 and 9 EeV curves depicted in Fig. 5.8 together with curve corresponding to 3 EeV were produced.

For higher energy region, where events are reconstructed with better precision, the differences between individual curves decreases. In the lower energy region it is necessary to compare these curves above given low energy cut. Considering this fact, the stability of the calibration curve may be assumed to be within 10 % wrt. change of low energy cut from the region 3 EeV to 9 EeV. Cuts of higher energy looses their reliability due to lack of events and thus they were not performed.

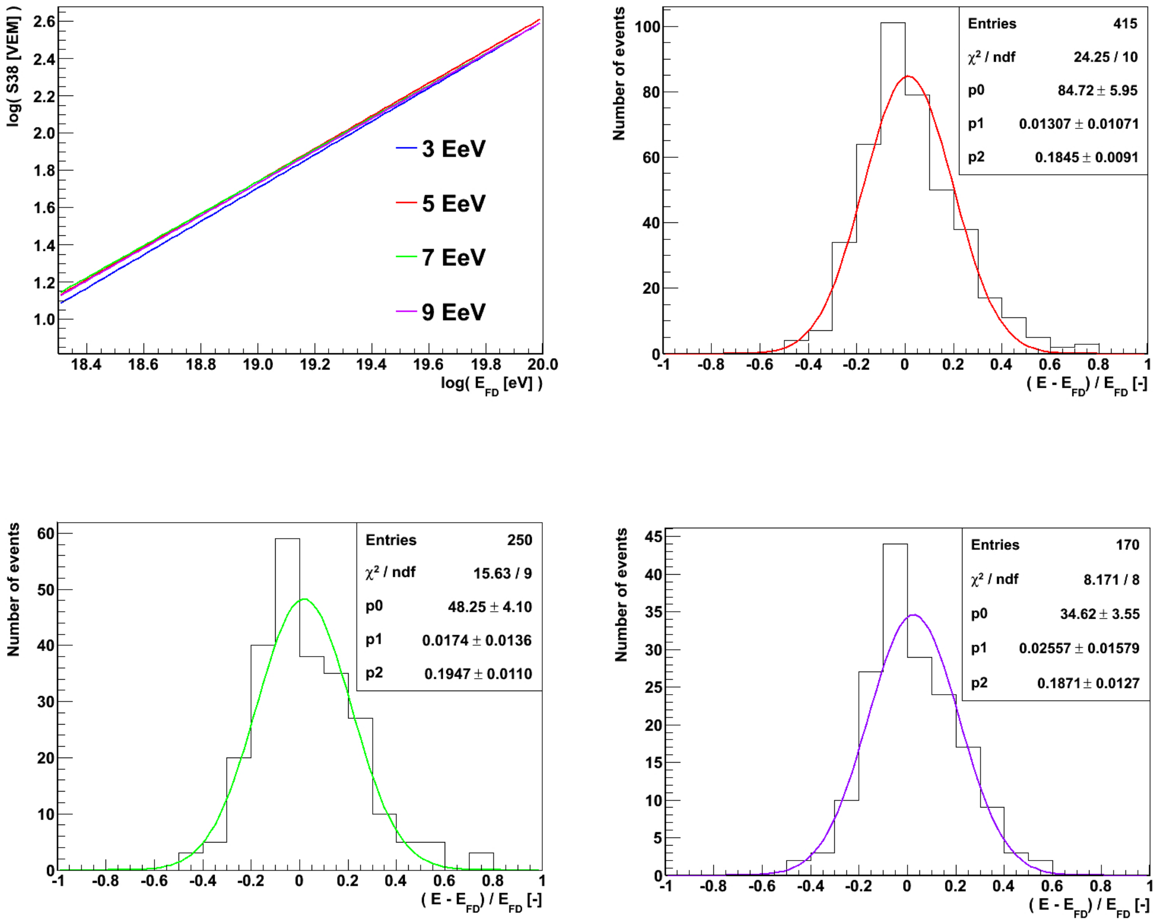

Figure 5.8: **Top left:** SD calibration curve obtained using different value of energy cut as it is indicated. Calibration from Fig. 4.9 was used for energy cut 3 EeV. **Other:** Histograms showing distribution of relative differences of E_{FD} from calibrated SD energy (E) relative to E_{FD} for 5 EeV (**Top right**), 7 EeV (**Bottom left**) and 9 EeV (**Bottom right**). Fitted gauss distributions with corresponding parameters are shown.

5.2.2 Is There Calibration Curve Dependence on Mass of Primary Particle?

To answer this question predictions of X_{max} dependence on energy E for proton and iron according to hadronic model EPOS were used. This dependence is predicted to be logarithmic in energy. Thus, a line (Fig. 5.9) was estimated in the middle between proton and iron linear dependencies (EPOS model) in Top Fig. 3.16. Following parameters of the line were chosen:

$$X_{max}[g \cdot cm^2] = 63 \cdot log(E[eV]) - 451.2\,. \tag{5.2}$$

The exact choice of parameters in eq. (5.2) is not crucial. The idea lies in dividing events to "lighter" (larger X_{max}) and "heavier" (smaller X_{max}). The calibration curve was drawn separately for events below this "boarder line" and for events above the line. Moving this boarder line lower in the graph, the selected events below the shifted line should contain larger fraction of showers induced by heavy primaries. Similarly this line was moved upward to select showers induced by lighter primaries. Naturally, moving this cut line from the middle, data set of events used for drawing of calibration curve decreases and so does also the precision.

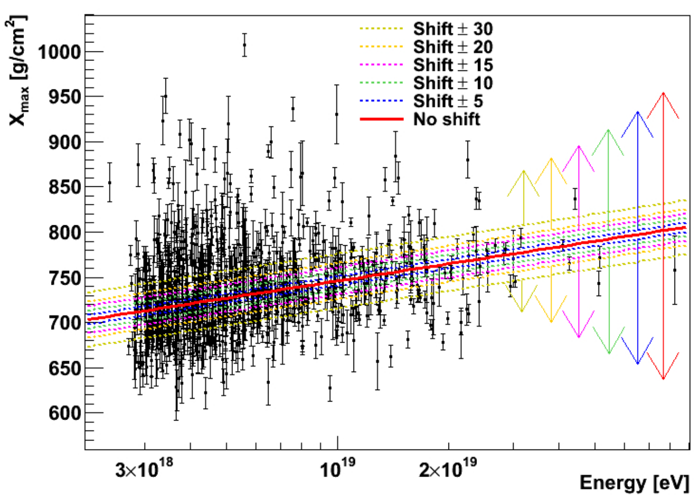

Figure 5.9: Dependence of X_{max} on energy for events used for drawing Fig. 4.9. Line corresponding to the expected behaviour of proton-iron averaged mixture according to EPOS is shown together with its shifts.

In Fig. 5.10 different calibration curves are shown using mentioned selection criteria. All curves derived from events of larger X_{max} are situated below the calibration curve of all events and all curves calculated from events of smaller X_{max} lie above it. It suggests that there is a systematic shift between these curves depending on X_{max} cut. Greater deviations of calibration curve are seen for events of higher X_{max} for higher energies but in this region there is too small event statistics to make clear conclusions. On the other hand, curves at lower energies, where more events are used for calibration, show quite good stability of the calibration curve also for assumed different X_{max} cuts.

Another way of studying calibration curve stability wrt. X_{max} lies in the distribution of events around the central curve. Already mentioned relative differences of FD energy from calibrated energy were used. The SD energy was calculated according to universal calibration curve independent on X_{max} from Fig. 4.9. In the Fig. 5.11 these distributions are shown for events occurring above the boarder line and boarder line shifted upwards (light nuclei).

A negative shift of the mean value of $(E - E_{FD})/E_{FD}$ distribution is visible. It can be caused by two effects. At first, the shape of attenuation curve for deeply penetrating showers (light nuclei) can be different than the CIC curve obtained from whole data set. Secondly, the missing energy correction actually applied when calculating E_{FD} is larger than it should be for light nuclei. Hence E_{FD} is systematicaly overestimated and thus $(E - E_{FD})/E_{FD}$ is naturaly shifted to negative values.

The same method was applied to events located below the boarder line and corresponding shifts of this line downwards (Fig. 5.12). On the contrary to events of greater X_{max}, a positive shifts of centers of gaussians is observed in $(E-E_{FD})/E_{FD}$ distributions for events with small X_{max} values. The size of the shift increases with decreasing X_{max} values. This can be explained by underestimation of E_{FD} due to too small missing energy correction applied for these showers. A well preserved gaussian shape of distributions can indicate either symetric nature of shower-to-shower fluctuations or eg. a presence of only one dominant type of heavier nuclei.

All together, the behaviour of distributions $(E - E_{FD})/E_{FD}$ and calibration curve was found to be sensitive to X_{max} values and thus to chemical composition of primary cosmic rays.

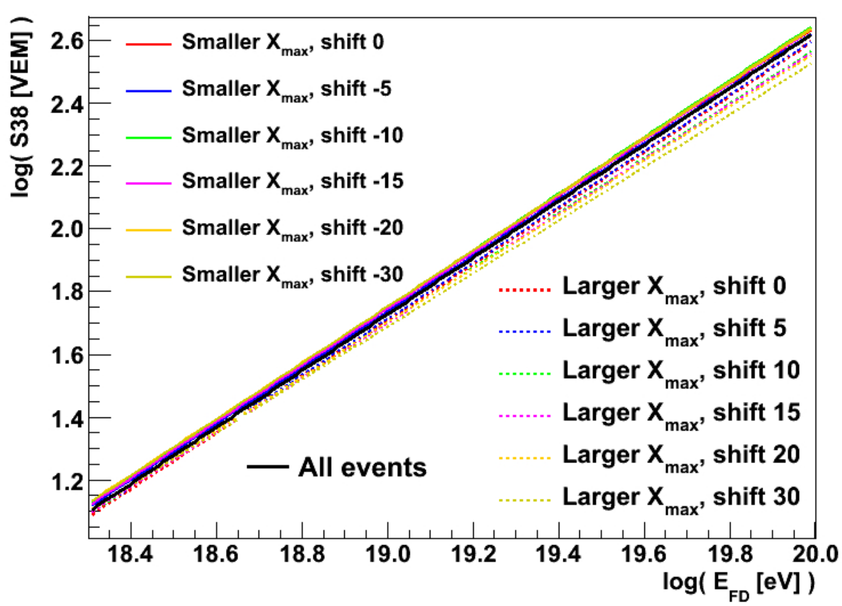

Figure 5.10: Calibration curves drawn from events according their position wrt. the boarder line (see text). For comparison, calibration curve from Fig. 4.9 is depicted too.

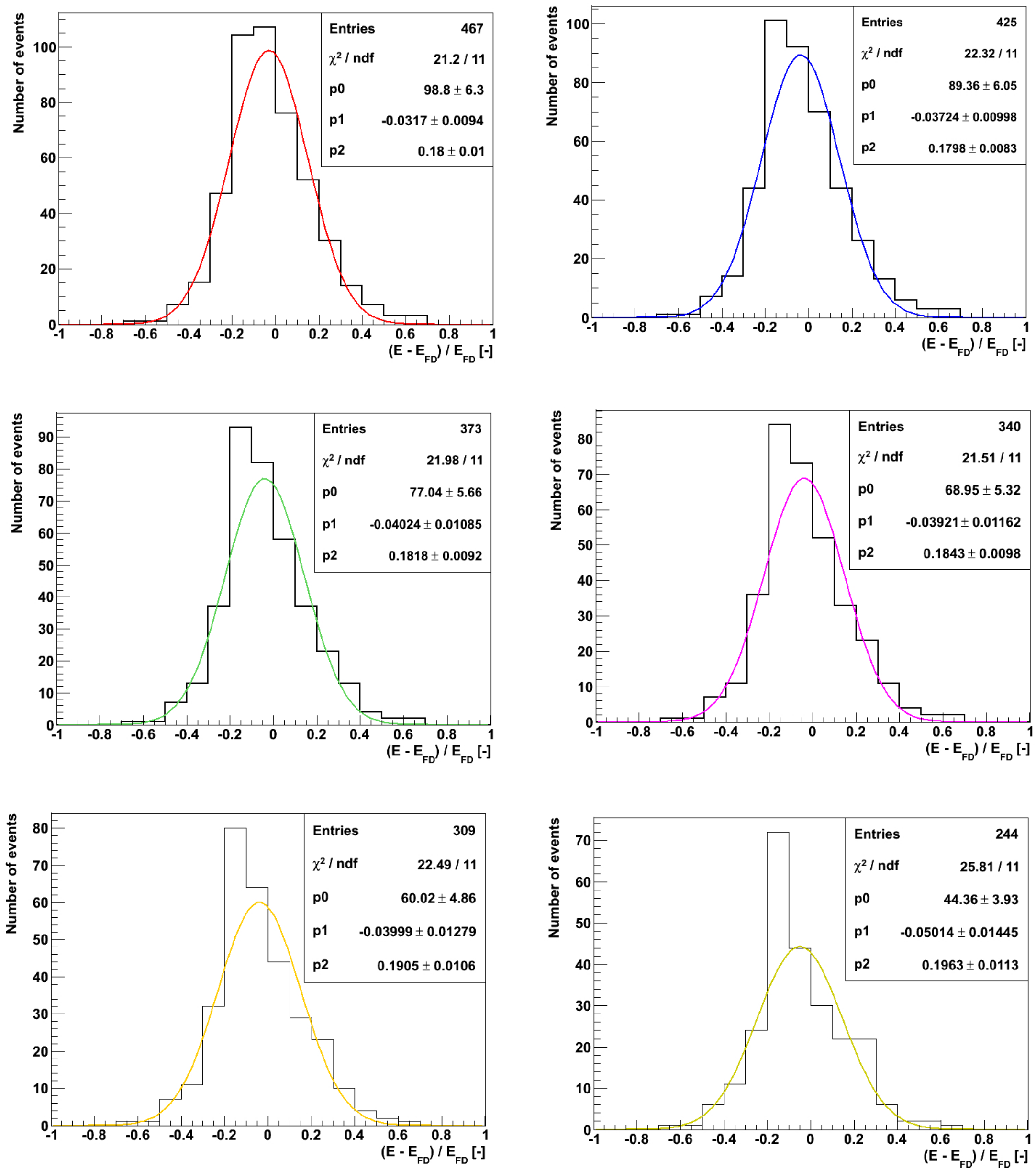

Figure 5.11: Histograms showing distribution of relative differences of E_{FD} from calibrated SD energy (E) relative to E_{FD} for different value of boarder curve shift (see text). Events lying above the boarder line without shift (**Top left**), shifted of 5 g·cm^{-2} (**Top right**), of 10 g·cm^{-2} (**Middle left**), of 15 g·cm^{-2} (**Middle right**), of 20 g·cm^{-2} (**Bottom left**) and of 30 g·cm^{-2} (**Bottom right**) are depicted. The negative shift of mean value ($p1$) with increasing shift of boarder line is obvious.

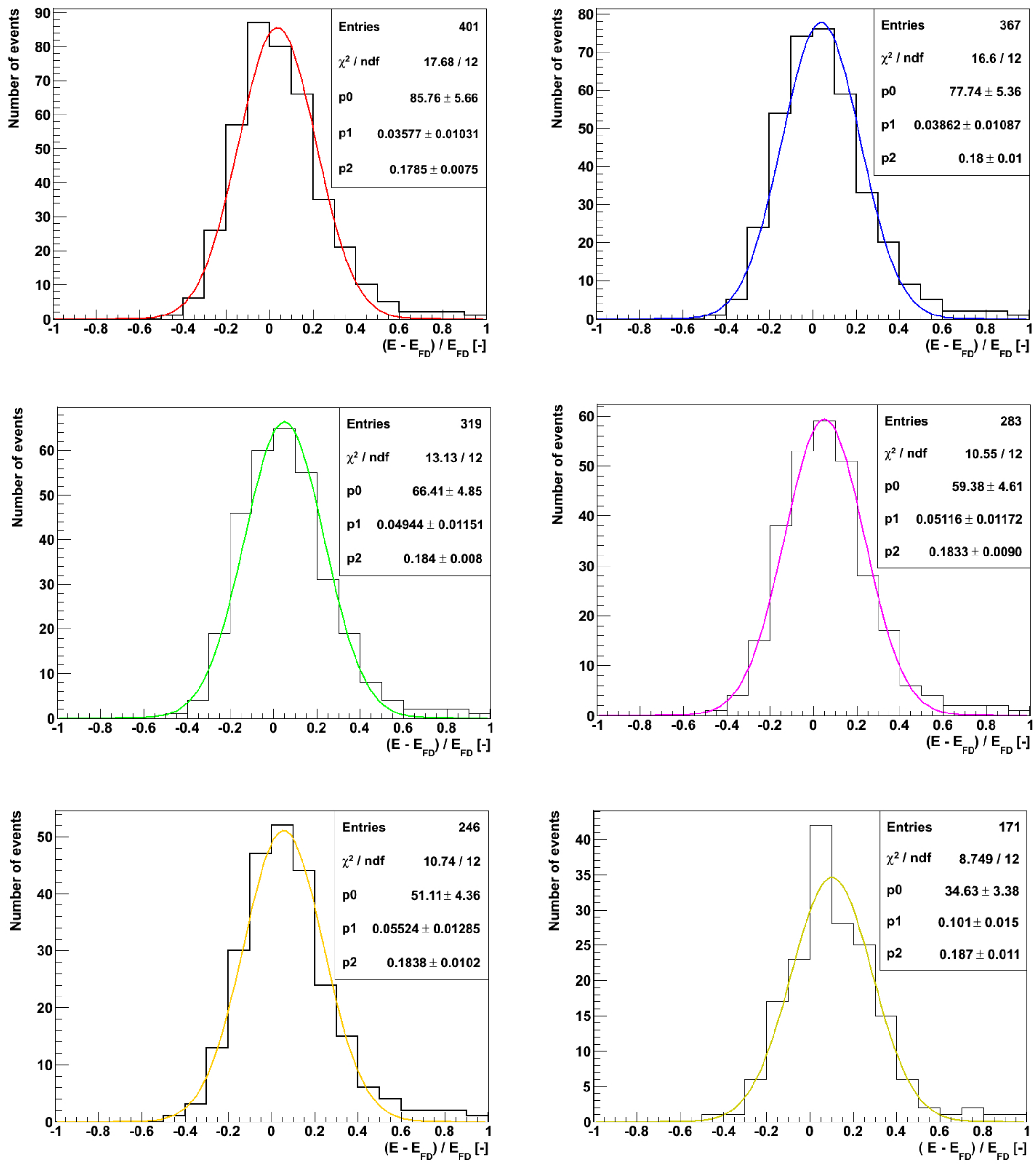

Figure 5.12: Histograms showing distribution of relative differences of E_{FD} from calibrated SD energy (E) relative to E_{FD} for different value of boarder curve shift (see text). Events lying below boarder line without shift (**Top left**), shifted of -5 g·cm^{-2} (**Top right**), of -10 g·cm^{-2} (**Middle left**), of -15 g·cm^{-2} (**Middle right**), of -20 g·cm^{-2} (**Bottom left**) and of -30 g·cm^{-2} (**Bottom right**) are depicted. The positive shift of mean value ($p1$) with decreasing shift of boarder line is obvious.

5.2.3 Comparison of Individual Eyes

Due to lack of absolute calibration at FD station at Loma Amarilla, only data from remaining three FDs passed required cuts. Independent SD calibrations for individual eyes were performed in Fig. 5.13. Resulting calibration curves shows good mutual correlation, which confirms calibration curve stability again. From relative differences between calibrated energy and FD energy distributions it follows, that FD station at Coihueco meets the gauss distribution with the shortest width (Tab. 5.1). Thus it seems that Coihueco provides better FD measurement wrt. rest two stations. There is a different type of mirror segment shape used at Coihueco's telescopes on the contrary to Los Leones and Los Morados, which may be responsible for more precise measurement at Coihueco FD station.

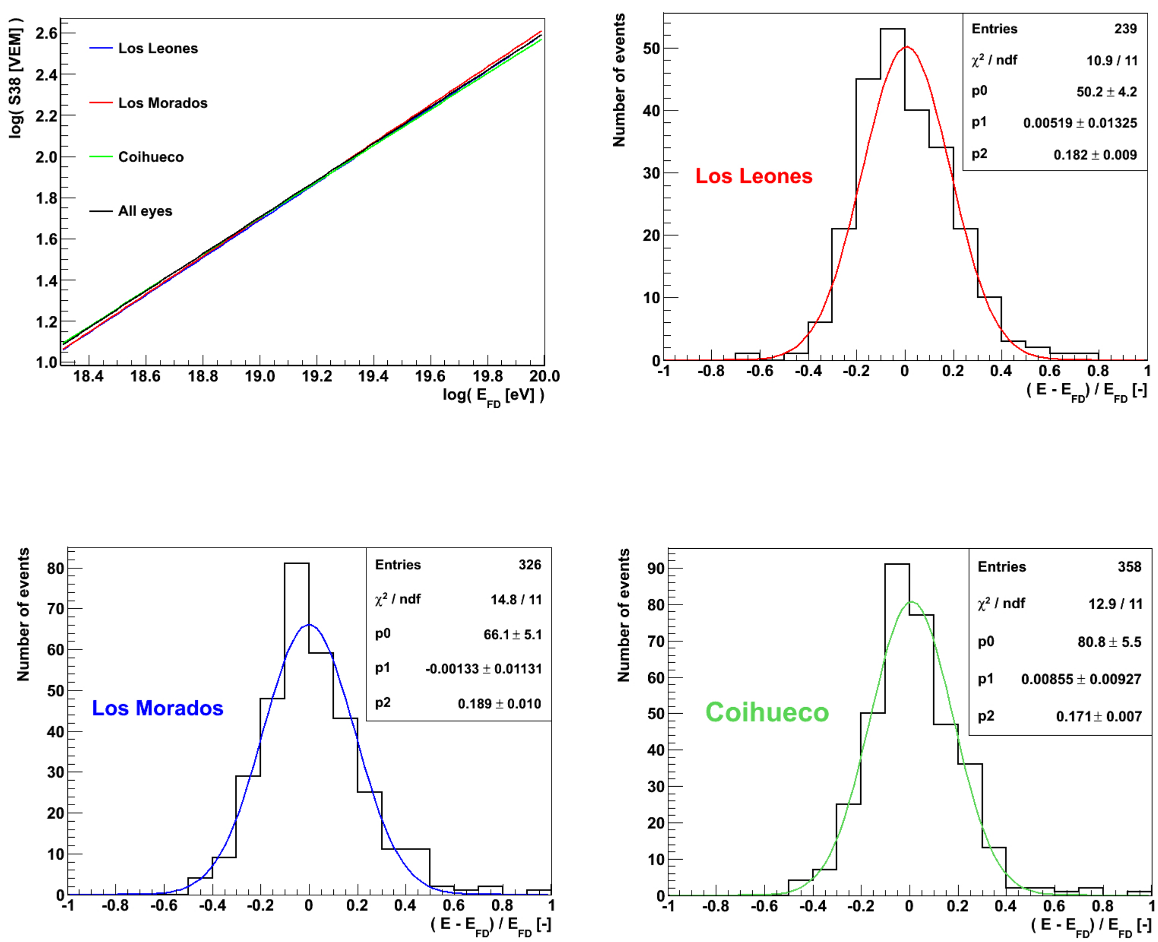

Figure 5.13: **Top left:** SD calibration curve obtained using FD data from individual eyes of FD. For comparison, the curve from Fig. 4.9 is also shown. **Other:** Histograms showing distribution of relative differences of E_{FD} from calibrated SD energy (E) relative to E_{FD} for Los Leones (**Top right**), Los Morados (**Bottom left**) and Coihueco (**Bottom right**). Fitted gauss distributions with parameters are shown.

Eye name	**a [10^{17} eV]**	**b [-]**	**Mean [%]**	**width [%]**
Los Leones	1.23 ± 0.29	1.093 ± 0.001	0.5 ± 1.3	18.2 ± 0.9
Los Morados	1.46 ± 0.32	1.089 ± 0.009	-0.1 ± 1.1	18.9 ± 1.0
Coihueco	1.18 ± 0.23	1.131 ± 0.009	0.9 ± 0.9	17.1 ± 0.7

Table 5.1: Constants of energy calibration, eq. (4.4), obtained by individual eyes of FD. The position of mean value and width of corresponding gauss distributions are also shown.

5.2.4 Seasonal Variances

As it was indicated for attenuation curve, the actual atmosphere conditions have an influence on shower detection. Despite the fact that for attenuation curve the variances were quite high, the calibration curve occur to be stable under various atmosphere conditions, which may be seen in Fig. 5.14 where relative differences of calibrated energy from FD energy were plotted with dependence on time of detection (t) during year. A fit with sinus function

$$\frac{E - E_{FD}}{E_{FD}} = a \cdot sin(b \cdot t + c) \tag{5.3}$$

was applied. Parameters a, c were set to be free but the parameter b was fixed to maintain year periodicity. The resulting amplitude (Tab. 5.2) shows maximal deviations ($\sim$ 4 %) from calibration curve during late summer and late winter, which indicates that seasonal variances of atmosphere can play some role. The stability of calibration curve during seasonal variable atmospheric conditions was thus estimated to be within 5 %.

a [%]	**b [month^{-1}]**	**c [-]**
4.2 ± 0.2	$2{\cdot}\pi/12$	0.33 ± 0.05

Table 5.2: Constants of fitted sinus curve described by eq. (5.3) in Fig. 5.14. The period parameter (b) was fixed to correspond to one year.

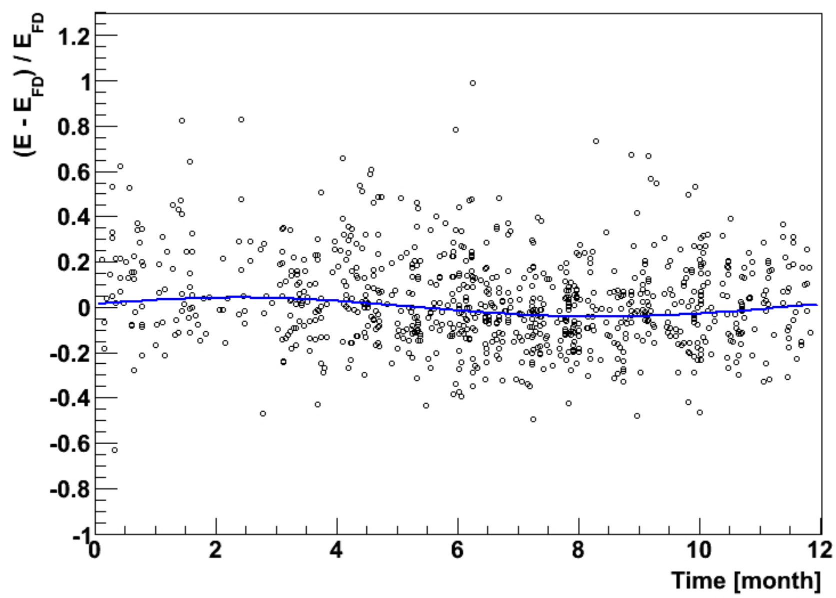

Figure 5.14: Relative differences of FD energy (E_{FD}) from calibrated energy (E) are shown with dependence on time of detection during year. Events used for drawing of Fig. 4.9 were used. Fitted sinus function is shown.

Chapter 6

Conclusions

This thesis was devoted to the energy calibration of the surface detector at Pierre Auger Observatory using high quality hybrid showers. Especially, various aspects of the energy calibration procedure were studied. For drawing and studying of attenuation and calibration curves data collected by PAO during more than 5 years were used. The comparison of these curves with official procedure of SD energy calibration at PAO showed reliability of the obtained results.

The attenuation curves derived applying modified CIC method independent on official procedure have proven to be only slightly dependent on chosen flux cut and size of bin $cos^2(\Theta)$. The attenuation curve reconstruction stability was estimated to be within 5 % for inclined and vertical shower. Using simulated showers induced by 10 EeV proton and iron for hadronic interaction model EPOS 1.66 discrepancies were found comparing simulated attenuation curves with curve derived from PAO data. The hadronic model EPOS 1.66 does not fully describe the shape of the attenuation curve from real data.

Influence of atmosphere density on attenuation curve was indirectly observed. The attenuation curve drawn from events detected during summer months showed a different attenuation of $S1000$ values with zenith wrt. other seasons.

The calibration curve was obtained employing two different sets of high quality cuts. Using condition demanding cloud coverage to be less than 25 %, good precision (17 %) comparable with official PAO calibration procedure was achieved. For studying detailed aspects of calibration procedure the mentioned condition was relaxed to obtain larger set of events for analysis. The stability of the calibration curve was shown for various lower energy cuts (3, 5, 7 and 9 EeV). The calibration curve obtained using individual FD eyes demonstrated mentioned stability again. About 4 % seasonal modulation of energy distribution around calibration curve was found.

Dependence of calibration curve on position of shower maximum was observed. When assuming universal calibration curve to be independent on X_{max}, deeply-penetrating/shallow showers are reconstructed on average with smaller/larger SD energy than is the value of energy given by FD. One suggested explanation is overestimation/underestimation of missing energy correction for light/heavy primaries measured by FD. This behaviour suggests that differencies between energies measured by FD and SD are sensitive to chemical composition of primary cosmic rays.

References

[1] Haungs A., Rebel H. a Roth M., *Energy spectrum and mass composition of high-energy cosmic rays*, Rept. Prog. Phys. 66 (2003), pp. 1145-1206.

[2] Ulrich R. M., *Measurement of the proton-air cross section using hybrid data of the Pierre Auger Observatory*, Doctoral thesis, GAP Note 2008-004, (2008).

[3] Protheroe J. R., *Acceleration and Interaction of Ultra High Energy Cosmic Rays*, ADP-AT-98-9 (1998), arXiv:9812055v1 [astro-ph].

[4] Prouza M., *Ultra-high Energy Cosmic Rays and Theirs Detection in AUGER Project*, Doctoral thesis at FMP UK in Prague, (2005).

[5] Hillas A. M., *Cosmic rays in an evolving universe*, Rev. Can. Phys. 46 (1968), pp. 623-626.

[6] Swordy S. P. et al., *Cosmic Rays at the Energy Frontier*, Sci. Am. 276 (1997), pp. 40-46.

[7] The Pierre Auger Collaboration, *Pierre Auger Design Report*, Fermilab, (1997).

[8] Nagano M. and Watson A. A., *Observation and implications of the ultrahigh-energy cosmic rays*, Rev. Mod. Phys. 72 (2000), p. 689.

[9] The HiRes Collaboration, *Observation of the Ankle and Evidence for a High-Energy Break in the Cosmic Ray Spectrum*, Phys. Lett. B619 (2005), pp. 271-280, arXiv:0501317v2 [astro-ph].

[10] Abraham J. et al., *Properties and performance of the prototype instrument for the Pierre Auger Observatory*, Nucl. Instrum. Meth. Phys. Res. A 523 (2004), pp. 50-95.

[11] Newton D., Knapp J., Watson A. A., *The Optimum Distance at which to Determine the Size of a Giant Air Shower*, Astrop. phys. 26 (2007), pp. 414-419, arXiv:0608118v1 [astro-ph].

[12] Bonifaci C. for the Pierre Auger Collaboration, *The angular resolution of the Pierre Auger Observatory*, Nucl. Phys. B 190 (2009), pp. 20-25.

[13] Allard D. et al., *Aperture calculation of the Pierre Auger Observatory surface detector*, 29^{th} International Cosmic Ray Conference Pune 7 (2005), pp. 71-74, fra-parizot-E-abs1-he14-poster.

[14] The Pierre Auger Collaboration, *The Fluorescence Detector of the Pierre Auger Observatory*, to appear in Nucl. Instrum. Meth. Phys. Res. A (2010), arXiv:0907.4282v1 [astro-ph.IM].

[15] Nagano M., *New measurement on photon yields from air and the application to the energy estimation of primary cosmic rays*, Astropart. Phys. 22 (2004), pp. 235-248.

[16] Kuempel D., Kampert K. H. and Risse M., *Geometry reconstruction of fluorescence detectors revisited*, Astropart. Phys. 30 (2008), pp. 167-174, arXiv:0806.4523v2 [astro-ph].

[17] Mostafa M., *The Hybrid Activities of the Pierre Auger Observatory*, Nucl. Phys. Proc. Suppl. 165 (2007), pp. 50-58, arXiv:0608670v1 [astro-ph].

[18] The Pierre Auger Collaboration, *Measurement of the energy spectrum of cosmic rays above* 10^{18} *eV using the Pierre Auger Observatory*, Phys. Lett. B 685 (2010) 239-246, arXiv:1002.1975v1 [astro-ph.HE].

[19] The Pierre Auger Collaboration, *The Cosmic Ray Energy Spectrum and Related Measurements with the Pierre Auger Observatory*, Presentations for the 31^{st} International Cosmic Ray Conference, Lodze, Poland (2010), http://www.auger.org/technical_info/ICRC2009/arxiv_spectrum.pdf.

[20] The Pierre Auger Collaboration, *Correlation of the Highest-Energy Cosmic Rays with Nearby Extragalactic Objects*, Science 318 (2007), pp. 938-943, DOI: 10.1126/science.318.5852.896.

[21] The Pierre Auger Collaboration, *Astrophysical Sources of Cosmic Rays and Related Measurements with the Pierre Auger Observatory*, Presentations for the 31^{st} International Cosmic Ray Conference, Lodze, Poland (2010), http://www.auger.org/technical_info/ICRC2009/arxiv_astrophysics.pdf.

[22] Ravignani D., Melo D. et al., *Infill Event Reconstruction*, GAP note 2009_116, (2009).

[23] The Pierre Auger Collaboration, *Studies of Cosmic Ray Composition and Air Shower Structure with the Pierre Auger Observatory*, Presentations for the 31^{st} International Cosmic Ray Conference, Lodze, Poland (2010), http://www.auger.org/technical_info/ICRC2009/arxiv_composition.pdf.

[24] The Pierre Auger Collaboration, *Measurement of the Depth of Maximum of Extensive Air Showers above* 10^{18} *eV*, Phys. Rev. Lett. 104 (2010), pp. 1-7, arXiv:1002.0699v1 [astro-ph.HE].

[25] The Pierre Auger Collaboration, *Upper limit on the cosmic-ray photon fraction at EeV energies from the Pierre Auger Observatory*, Astropart. Phys. 31 (2009), pp. 399-406.

[26] Pierog et al., *Latest Results from the Air Shower Simulation Programs CORSIKA and CONEX*, arXiv:0802.1262v1, (2008).

[27] Cronin J. W., Yamamoto T., *Simulation-independent determination of the cosmic ray spectrum for energies above* $2 \cdot 10^{18}$ *eV*, draft version (2006).

[28] The Pierre Auger Collaboration, *Atmospheric effects on extensive air showers observed with the Surface Detector of the Pierre Auger Observatory*, Astropart. Phys. 32 (2009), pp. 89-99, arXiv:0906.5497v2 [astro-ph.IM].